A Study of Light-Matter Interaction in Mesoscopic Region by Maxwell-Schrödinger Hybrid Simulation

（Maxwell-Schrödinger 方程式混合数値解析法による

メゾスコピック領域における光と物質の相互作用に関する研究）

January 2016

The Electrical Engineering Major

Graduate School of Science and Technology (Doctoral Course)

Nihon University

Takashi Takeuchi

Abstract

In this dissertation the author theoretically studies with respect to "*light-matter interaction*" by employing recently developed highly-accurate Maxwell-Schrödinger hybrid simulation that describes the mutual interaction procedure by solving Maxwell's and Schrödinger equations for light and matter, respectively. His research interest is particularly stirred up to physical phenomena which cannot fully described by not only the classical but also quantum theories, that is, he expediently expresses the region involving such phenomena as "*mesoscopic*" whose general definition is the middle region between macroscopic- and microscopic- ones.

The author investigates with respect to two typical problems characterized by light-matter interaction in mesoscopic phenomena by (i) many-electron systems and (ii) single-electron ones. Conventional theoretical models are employed to make comparisons with his more precise Maxwell-Schrödinger multi-physics simulation. As a result observed trends indicate qualitative differences obtained from those computational results and the importance of our hybrid simulation for investigating and clarifying the mesoscopic phenomena.

Acknowledgements

First of all I am deeply grateful to my parents. My student life has been always supported by their help. My scientific interests have originated from my further. My mother's dedicated support has allowed me to concentrate my research.

I would like to offer my special thanks to Professor Shinichiro Ohnuki who have kindly supervised me for a long period of time. Particularly during both M.S. and B.S., I could well-learn with respect to classical electromagnetic dynamics and the research ways, from him, that strongly take root in my basis.

I would like to express my greatest gratitude to Professor Tokuei Sako who leads me to the way of researchers by showing his profound knowledge of physics to describe light-matter interaction in a quantum world and by teaching sophisticated academic manner, culture, and history. My research would not come into existence without his great contribution.

I would like to show my appreciation to Professor Katsuji Nakagawa and Yoshito Ashizawa who have given me a number of helpful questions, comments, and discussions, especially in terms of engineering view, that make my scientific sense wide.

Finally I owe my gratitude to Professor Tsuneki Yamasaki. He have always given me many kind advices relevant to my research and life.

Contents

1 Introduction

1.1 Research background

In present-day society the information technologies have played a significantly important role as a basis strongly supporting our life which has been further rapidly sophisticated especially over last three decades. Such fast-growing advancements in Japan have started from 1985 when Nippon Telegraph and Telephone Public Corporation has privatized as NTT(:Nippon Telegraph and Telephone Corporation) and, after that, a competition principle has been introduced into domestic- and international-telecommunications markets in the country, leading to drastic developments in the information and communication industry [1]. During the passionate three decades the information equipment and system have made remarkable progress, such as a telephone transceiver, personal computer, mobile phone currently called as smartphone, optical transmission system, and so on.

In a wide perspective a key ingredient of their functionalities carving out the forefront of information technologies is based on the so-called "*light-matter interaction*" in which matter is affected by the electromagnetic field, through the Lorentz's force in a classical mechanical sense, and light is affected by electrical current excited from the matter. Particularly in recent studies utilizing the interaction in an ingenious way, some interesting phenomena and technologies have been actively proposed and studied as follows:

(i) Plasmonic device

Precious metals such as silver and gold have negative complex permittivity strongly interacting with laser fields especially in a visible light band from around 400 nm to 800 nm since almost numberless conduction electrons in the metals subjected to external electromagnetic fields are resonated for the band. The permittivity particularly for the case of nano-scale objects is well-known to excite collective oscillatory motion of a large number of the electrons, namely *plasmon*, and enables us to enhance and localize the electromagnetic energy around the nano objects into a significantly minuscule region smaller than the wave length of light in spite of the fact that usually the electromagnetic energy cannot be concentrated into a such region because of diffraction limitation of light. This enhanced and extremely localized electromagnetic energy based on light-matter interaction has been expected to apply to various next-generation key technologies in a wide range of areas, such as ultra-high sensitivity sensors [2] and significantly compact circuit combining photonics and electronics, namely plasmonic circuits [3]. Furthermore, also from perspective of information storage, such a way to highly concentrate electromagnetic energy by

4

plasomonic devices has attracted great interest, for instance a heat assisted magnetic recording system that is one of novel high density magnetic recording systems effectively using heat whose spot size directly determines the recording density and can be condensed to fine region by plasmon [4].

(ii) Quantum computer

Although existing all conventional computers so far, that is, "classical computers", have employed a certain operating system to the elementary component determining only 0 or 1, a quantum computer utilizes the superposition of discrete quantum levels of a particle, namely *q-bits*, such as an electron, an atom, and a molecule. The parallelism of current classical supercomputers are restricted to almost 2^{20} whereas one of the quantum computer is 2^n for the case of n q-bits operating system, enabling significantly ultra-high speed computation if n being well over 20 can be realized. The first groundbreaking study with respect to the quantum computer was done by P. Benioff in 1980 when he theoretically presented that quantum systems could be utilized to computation without energy loss [5]. Also R. Feynman has discussed with respect to the quantum computer in 1982 when he suggests that it is exponentially faster than the classical computational systems [6]. After these innovative studies P. W. Shor has proposed novel functional algorithm that has attracted a tremendous attention to a study of quantum computation [7]. Through such fundamental and theoretical approaches, great efforts have been devoted to actually realize the quantum computer as a hardware system. Their representative examples are known as some adroit methodologies such as systems relying on the use of nuclear magnetic resonance [8], superconducting quantum interference devices [9], and quantum dots [10]. In addition to these a system much further directly utilizing light-matter interaction has been proposed and investigated, where a laser pulse is designed under an optimal control theory (called "*light control pulse*" hereafter) and operates the target quantum states [11-13].

The key ingredient of both above-mentioned topics is "*light-matter interaction*" which enables nano-scale objects consisted of precious metals, plasmonic devices, to generate strongly enhanced and localized electromagnetic fields while allows quantum computers, particularly for systems driven by light pulses, to control the discrete quantum levels. We, however, can notice that those interactions require us to carefully deal with their theoretical models because they involve some combined complex physical natures raging from macroscopic- to microscopic-phenomena (detail explanation is described in the next subsection 1.2 Research purpose). More strictly speaking they need us to introduce "*multi-physics theory*" composed of classical- and quantum theories. In this dissertation the author expediently describes such situation as "*mesoscopic*", hereafter, whose general definition is the middle region between macroscopic- and microscopic- ones.

Unfortunately, the almost phenomena observed in the mesoscopic region is still beyond the understanding of the newest theoretical works and known as mysterious mechanism since mesoscopic physics cannot be rationalized by only either classical- or quantum-theories in straight forward ways. Therefore, very recently, some novel approaches relying on computational simulation to investigate the mesoscopic phenomena have been proposed and actively discussed by our [14-16] and other groups[17-19], where we employ *multi-physics* treatment to efficiently and accurately model the light-matter interaction, namely hybrid simulation of Maxwell-Schrödinger equations. This groundbreaking hybrid scheme utilizes both classical- and quantum-theories to describe light and matter behaviors, respectively, and has been successfully applied to performing some numerical mesoscopic simulations: nonlinear propagation of attosecond pulses generated by high harmonic emissions [17], H_2^+ gas interacting with ultrashort laser pulses [18], and a carbon nanotube transistor [19].

1.2   Research purpose

This dissertation discusses with respect to the following topics, deeply relevant to plasmonic devices and quantum computers driven by light control pulses, in which the author makes a comparison between their conventional theoretical frames and his Maxwell-Schrödinger one, indicating qualitative differences observed by those computational results and the importance of multi-physics simulation for investigating and clarifying the mesoscopic phenomena:

1. Light-matter interaction: many-electron systems

Plasmonic devices to enhance and localize electromagnetic energy into a very small region are nano-scale objects composed of precious metals including an enormous amount of electrons constrained in the electrostatic potentials. Their conventional theoretical models are exclusively treated by solely classical theory so far, namely Maxwell-Newton approach, in spite of the fact that the devices have intricate nature characterized by not only classical- but also quantum-physics. Current some works [20, 21], thus, have actually revealed the inconvenient limitation for the conventional treatment by their experimentations where the theoretical results obtained by conventional Maxwell-Newton approach starts to deviate from the actual experimental ones particularly as the plasmonic devices become small from tens of nano meter to sub-nano meter scale. The main reason of such deviation is based on the lack of the quantum mechanical consideration for the modelling of the electrons in the devices. Therefore, very recently, far-seeing research groups [22, 23] have proposed a new theoretical optical response model, called a hydrodynamic Drude model, that takes into account a part of such mesoscopic problems composed of the classical- and quantum natures by incorporating the viscosity of collective

electrons with fitting parameters from experimentations. Although their new method does not fully model quantum-mechanical effects, as a result they have succeed to verify the reasonability of the method by making a comparison with the conventional Maxwell-Newton one in terms from the scale of the plasmonic devices raging tens of nano meter to sub-nano meter.

As with above previous studies the author's purpose here is also to investigate and clarify light-matter interaction by many-electron systems as in plasmonic devices, but we especially focus on the potential structure that confines the electrons and is so far modelled by a purely harmonic oscillator though those can be extracted to have disarray, namely the *anharmonicity* of the potential, particularly around the surface of the plasmonic devices where many plasmon electrons especially concentrate [14, 15]. The author, therefore, has utilized the hybrid simulation of Maxwell-Schrödinger equations and studied a system of a nano-scale thin film, assumed as the surface of plasmonic devices, interacting with pulsed laser fields, where the electrostatic confining potential for the electrons is characterized by *locally* and *globally* anharmonicities. Furthermore in order to carefully discuss mesoscopic phenomena for this case, conventional Maxwell-Newton approach also have been employed to make a comparison with Maxwell-Schrödinger one. Resultant observed trends from these two distinct hybrid simulations have enabled us to find some typical differences that deeply depends on the structure of electrostatic potential.

2. Light-matter interaction: single-electron systems

Modulated ultrashort laser pulses designed under an optimal control concept have potential ability to transfer completely probability densities among discrete quantum states of matter to an arbitrary desired state [24-26]. This pioneering technology has attracted great attention over the last two decades since it can be used in quantum computation in which q-bits realized in discrete quantum levels are processed by external laser pulses [11-13]. Although possibility in controlling quantum states of molecules has been demonstrated in actual experiments by generating laser pulses using a generic algorithm and finding an optimal pulse [27-29], such approaches require us to conduct very high-cost experimentations through hundreds of accumulated trials and errors. This thing clearly indicates the need of theoretical ways to obtain such tailored laser pulses and has let previous vigorous researchers develop the innovative pulse designing scheme where the key ingredient here is the so-called optimal control theory which can lead an optimal laser pulse, namely light control pulse [30-32].

We, however, note here that the previous innovative theoretical studies on light control pulses conducted so far have, to our best knowledge, exclusively relied on the assumption that the electromagnetic field near the target system is not disturbed by the excitation of electrons. Assuming that an atom or a molecule in its electronic ground state is irradiated by a pulsed laser field. When the incident laser pulse with an appropriate central frequency for exciting the target

system arrives, the atom or molecule becomes a time-dependent superposition of the ground and some excited states, or in a classical mechanical sense, the electrons in the system are forced to move back and forth along the polarization direction of the laser light by its alternating electric field. This forced-oscillatory motion of electrons becomes a local polarization current source and radiates a new electromagnetic field. Then, the electromagnetic field near the target system should become the sum of the original incoming wave and the induced new one, that interacts again with the target repeating the cycling processes of excitation and radiation. This modification of the laser field by the induced radiation from the excited electrons has been considered so far as being negligibly small particularly for the cases of isolated atoms and molecules since their number of electrons is much smaller than the number of photons in the laser pulses. This approximation has allowed one to facilitate easily designing light control pulses. On the other hand, since excited electrons could yield a locally strong electromagnetic field, sometimes referred to as a 'near field', in the vicinity of the electrons themselves [33-35], its validity of omission of the induced radiation needs to be verified carefully. In other words this problem can be classified as mesoscopic since reasonable physics then should be described by taking into account both the target quantum system and total laser field involving incident optimal pulse and newly generated near field. Therefore hybrid simulation of the coupled Maxwell-Schrödinger equations is the most straightforward way to check this validity, where the feedback from the electrons to the electromagnetic field is incorporated by adding to Maxwell's equations a polarization current density that is obtained from the time-dependent wave function of the electrons.

The author's purpose here is to investigate and clarify the effect of the near field into a target system, by employing the hybrid simulation of Maxwell-Schrödinger equations, which is chosen as a single electron confined in a quasi-one-dimensional nanoscale structure modelling quantum dots with a light control pulse designed by the conventional method relying on the approximation. In addition to the verification for conventional scheme the author will propose a novel method to design a light control pulse which precisely takes into account the interaction consisted of near field owing to the Maxwell-Schrödinger algorithm [16].

1.3   Overview

This dissertation is organized as follows.

Section 2 discusses with respect to light-matter interaction by many-electron systems. The first subsections 2.1 describes our theoretical model, computational details for Maxwell-Schrödinger and -Newton hybrid simulations, and how to implement these two distinct schemes in computer codes based on the so-called finite-difference time-domain (FDTD) method. The next subsection 2.2 represents our computational results. We will show three types of examples for the

electrostatic potentials confining electrons: (a) purely harmonic (b) locally anharmonic (c) globally anharmonic. Resultant trends for these potentials indicate some crucial qualitative differences between conventional Maxwell-Newton and our precise Maxwell-Schrödinger schemes. The observed differences are due to the typical quantum mechanical effects occurred by the anharmonicity of the confining potential structure. We briefly summarize those results in the subsection 2.3.

Section 3 discusses with respect to light-matter interaction by single-electron systems. The first subsections 3.1 describes our theoretical model and computational details for hybrid simulation of Maxwell-Schrödinger equations and designing scheme of conventional light control pulses. The next subsection 3.2 represents our computational results. We will show here that even in the case of systems with a single electron the induced radiation from the excited electron cannot be negligible, that could substantially modify the original incoming electromagnetic fields locally. This leads to significantly low control ability of the conventional pulse particularly when the local electron density is large. Furthermore also new light control pulse designed by our proposed designing scheme has been verified, indicating stable control accuracy owing to consideration for light-matter interaction in the scheme. We briefly summarize those results in the subsection 3.3.

Finally the author comprehensively concludes his thesis in the section 4.

1.4   Technical symbols and terms

The technical symbols and variables appeared into this dissertation are explained in the following list.

Symbols and variables	Explanations
$\Delta x, \Delta y, \Delta z$	Discrete intervals for the x-, y-, and z-axes
Δt	Discrete intervals for the time axis
i, j, k	Indices for the space grids for the x, y, and z axes
n	Index for the time step
$i_{max}, j_{max}, k_{max}$	Number of grid points for i, j, and k
m	Mass of an electron
q	Charge of an electron
$\hbar$	Dirac constant
ε_0	Permittivity of vacuum
μ_0	Permeability of vacuum
c	Light speed in vacuum
$\mathbf{E}$	Electric field
$\mathbf{H}$	Magnetic field
ψ	Wave function

2   Light-matter interaction: many-electron systems

A novel hybrid simulation based on the coupled Maxwell-Schrödinger equations has been utilized to investigate, accurately, the dynamics of so many electrons confined in a one-dimensional potentials and subjected to time-dependent electromagnetic fields, where this studied system is modelled to assume the surface of plasmonic devices. A detailed comparison has been made for the computational results between the Maxwell-Schrödinger and conventional Maxwell-Newton approaches for some distinct cases, namely characterized by harmonic and anharmonic electrostatic confining potentials. The results obtained by the two approaches agree very well for the purely harmonic potential while disagree quantitatively for the anharmonic potential. This clearly indicates that the Maxwell-Schrödinger scheme is indispensable to study mesoscopic phenomena particularly when the anharmonicity effect plays an essential role.

2.1   Theoretical model and computational details

Figure 2.1 illustrates our theoretical model used in the present section. The thin film is uniform in the y-z plane and its optical properties are assumed to be calculated from the responses of one representative electron among a larger number of electrons comparable to the order of Avogadro's number. The incident laser fields consisting of only E_y and H_z components are given by a plane wave, which simultaneously excite all electrons in the film to the polarization direction y. Therefore, the computational model here can be significantly simply constructed by employing the one-dimensional models for both electrons and light. This effectively facilitated model enables us to solve both of Maxwell-Schrödinger and Maxwell-Newton equations very accurately and efficiently, allowing us a detailed comparison of their computational results. After this subsection the formulation based on FDTD algorithm [14-16, 18-19, 36-40] to solve the 1D-1D problem will be described.
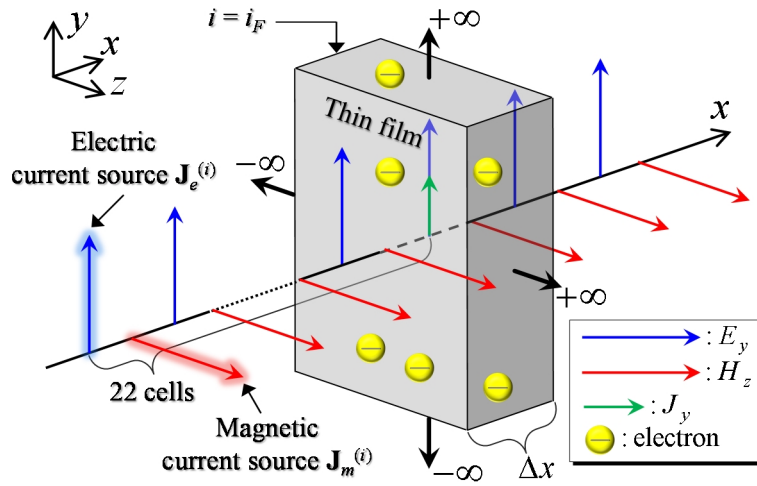
FIG. 2.1. The geometry and coordinate systems. A thin film assumed as the surface of plasmonic devices and current sources exciting a incident plan wave, illustrated by a grey box and blue arrows, respectively, are uniform in the *y-z* plane. All electrons in the film are confined in the electrostatic potential *V*, and can move along the *y* axis which is parallel to the direction of the electric field.

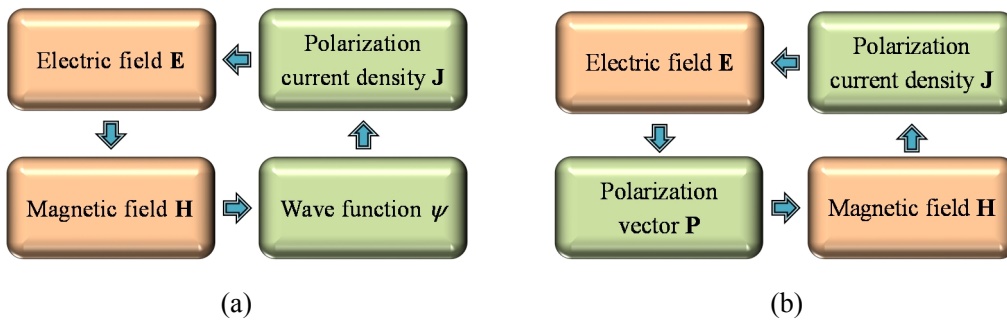(a)   (b)

FIG. 2.2. A schematic illustration of the computational schemes for the two hybrid simulations: Maxwell-Newton (a) and Maxwell-Schrödinger (b).

2.1.1 Maxwell-Schrödinger hybrid scheme for 1D-1D problems

The computational procedure to solve the Maxwell-Schrödinger hybrid scheme is schematically illustrated in Figure 2.2 (a). Maxwell's equations for dielectric objects are given by

$$\nabla \times \mathbf{E} = \mu_0 \frac{\partial \mathbf{H}}{\partial t}, \tag{2.1}$$

$$\nabla \times \mathbf{H} = \varepsilon_0 \frac{\partial \mathbf{E}}{\partial t} + \mathbf{J}, \tag{2.2}$$

where $\mathbf{J}$ represents the polarization current density defined by the time derivative of the polarization vector $\mathbf{P}$. Since the electromagnetic fields have only E_y and H_z components in the present section, they can be updated by the following recursion relations based on the Maxwell FDTD method [14-16, 18-19, 36-37, 40]:

$$H_z^{n+1/2}(i+1/2) = H_z^{n-1/2}(i+1/2) - \frac{\Delta t}{\mu_0 \Delta x}\left\{E_y^n(i+1) - E_y^n(i)\right\}, \tag{2.3}$$

$$E_y^{n+1}(i) = E_y^n(i) - \frac{\Delta t}{\varepsilon_0 \Delta x}\left\{H_z^{n+1/2}(i+1/2) - H_z^{n+1/2}(i-1/2)\right\} - \frac{\Delta t}{\varepsilon_0}\delta(i-i_F)J_y^{n+1/2}(i_F), \tag{2.4}$$

where i_F, and δ represents the cell position of the thin film and Kronecker delta function, respectively. The edges of computational domain in the Maxwell FDTD simulation are supplemented by the Mur absorbing boundary condition [37].

The Schrödinger equation for an electron subjected to a laser field is given by

$$i\hbar \frac{\partial \psi}{\partial t} = -\frac{\hbar^2}{2m}\nabla^2 \psi - q\mathbf{E} \cdot \mathbf{r} \psi + V\psi, \tag{2.5}$$

where V represents the confining electrostatic potential and the so-called length gauge has been adopted to describe the interaction between the electron and the electromagnetic field [41]. Since the electron simulated here has the degree of freedom for only the y-axis, the following recursion relations based on the Schrödinger FDTD method [14-16, 18-19, 38-39] can be obtained by separating the real and imaginary parts of the Schrödinger equation:

$$\psi_{imag}^{n+1/2}(j) = \psi_{imag}^{n-1/2}(j) + \frac{\hbar \Delta t}{2m}\alpha_j\left\{\psi_{real}^n(j)\right\} - \frac{\Delta t}{\hbar}\left\{V(j) - qY(j)E_y^n(i_F)\right\}\psi_{real}^n(j), \tag{2.6}$$

$$\psi_{real}^{n+1}(j) = \psi_{real}^n(j) - \frac{\hbar \Delta t}{2m}\alpha_j\left\{\psi_{imag}^{n+1/2}(j)\right\} + \frac{\Delta t}{\hbar}\left\{V(j) - qY(j)E_y^{n+1/2}(i_F)\right\}\psi_{imag}^{n+1/2}(j), \tag{2.7}$$

where ψ_{imag} and ψ_{real} are the imaginary and real parts of the wave function ψ with Y denoting the discretizing y-axis. The operator α_j in these equations performs the following sixth-order accurate difference to simulate the second-order derivative $\partial^2/\partial y^2$ for an arbitrary function F:

$$\alpha_\kappa\left\{F(\kappa)\right\} = \frac{1}{90\Delta_\kappa^2}\{F(\kappa+3) - 13.5F(\kappa+2) + 135F(\kappa+1)$$
$$- 245F(\kappa) + 135F(\kappa-1) - 13.5F(\kappa-2) + F(\kappa-3)\}, \tag{2.8}$$

where κ and Δ_κ correspond to one of $i, j,$ or k and one of $\Delta x, \Delta y,$ or Δz, respectively.

We employ the following Dirichlet boundary for the Schrödinger FDTD simulation:

$$\begin{cases} \psi(1) = \psi(2) = \psi(3) = 0, \\ \psi(j_{max} - 2) = \psi(j_{max} - 1) = \psi(j_{max}) = 0. \end{cases} \tag{2.9}$$

This condition is well-known to induce spurious oscillations when the wave function impinges on the boundary. Therefore, we utilize sufficient wide analysis domain so as to avoid these numerical artifacts.

The polarization current density $\mathbf{J}$ in the Maxwell-Schrödinger scheme is defined by the following expression with the electron density N:

$$\mathbf{J} = qN \int_{-\infty}^{\infty} \psi^* \frac{\hbar}{im} \nabla \psi \, d\upsilon. \tag{2.10}$$

Eq. (2.10) describes the average behaviour of the current density due to the motion of all electrons expressed by the wave function of a representative electron. The y component of (2.10) can be evaluated by

$$J_y^{n+1/2}(i_F) = \frac{qN\hbar\Delta y}{m} \sum_{j=4}^{K-3} \left[\psi_{real}^{n+1/2}(j)\beta_y\left\{\psi_{imag}^{n+1/2}(j)\right\} - \psi_{imag}^{n+1/2}(j)\beta_y\left\{\psi_{real}^{n+1/2}(j)\right\} \right] \tag{2.11}$$

where the operator β_y performs the following sixth-order accurate difference to simulate the first-order derivative $\partial/\partial y$ for an arbitrary function F.

$$\beta_\kappa\{F(\kappa)\} = \frac{1}{60\Delta_\kappa}\{F(\kappa+3) - 9F(\kappa+2) + 45F(\kappa+1)$$
$$- 45F(\kappa-1) + 9F(\kappa-2) - F(\kappa-3)\} \tag{2.12}$$

The Maxwell-Schrödinger hybrid scheme for 1D-1D problems can be operated by using Eqs. (2.3), (2.4), (2.6), (2.7), and (2.11) recursively as illustrated in Figure 2.2 (a).

2.1.2   Maxwell-Newton hybrid scheme for 1D-1D problems

The computational procedure adopted in the Maxwell-Newton scheme is shown in Figure 2.2 (b). The part for solving Maxwell's equations is the same as in the Maxwell-Schrödinger schemes based on (2.3) and (2.4). The following Newton equation is employed to describe the motion of a classical electron confined by the electrostatic potential V and subjected to an external electromagnetic field:

$$m\frac{d^2\mathbf{r}}{dt^2} = q\mathbf{E} + \mathbf{F}, \tag{2.13}$$

$$\mathbf{F} = -\nabla V, \tag{2.14}$$

where we assume that the electron feels no frictional force. The polarization vector $\mathbf{P}$ and polarization current density $\mathbf{J}$ in the Maxwell-Newton scheme [14-15, 40] are, respectively, defined by

$$\mathbf{P} = qN\mathbf{r}, \tag{2.15}$$

$$\mathbf{J} = \frac{\partial \mathbf{P}}{\partial t}. \tag{2.16}$$

Ones can derive the following recursion relations for simulating these polarization and current density in the FDTD framework as

$$J_y^{n+1/2}(i_F) = J_y^{n-1/2}(i_F) + \frac{qN\Delta t}{m}\left\{qE_y^n(i_F) + F_y^n(i_F)\right\}, \tag{2.17}$$

$$P_y^{n+1}(i_F) = P_y^n(i_F) + \Delta t J_y^{n+1/2}(i_F). \tag{2.18}$$

In the Maxwell-Newton scheme Eqs. (2.3), (2.4), (2.17), and (2.18) are solved recursively as displayed schematically in Figure 2.2 (b).

2.2 Computational results

The incident laser fields characterized by rather strong intensity are generated from the following electric and magnetic current sources $\mathbf{J}_e^{(i)}$ and $\mathbf{J}_m^{(i)}$ with the unit function $u(t)$

$$\mathbf{J}_e^{(i)} = \frac{J_0}{\Delta x \sqrt{\mu_0/\varepsilon_0}} \exp\left\{\left(\frac{t_0 - t}{\sigma_t}\right)^2\right\} u(t)\hat{\mathbf{a}}_y, \tag{2.19}$$

$$\mathbf{J}_m^{(i)} = \frac{J_0}{\Delta x (\mu_0/\varepsilon_0)} \exp\left\{\left(\frac{t_0 - t}{\sigma_t}\right)^2\right\} u(t)\hat{\mathbf{a}}_z, \tag{2.20}$$

where we have set J_0, Δx, σ_t, and t_0 as 1000 MA/m, 0.125 nm, 1.25 fs, and 20 σ_t fs, respectively. The time step Δt is chosen to be smaller by a factor of 0.9 than Δt_{CFL}, i.e., the maximum value allowed in the CFL condition [37], so as to guarantee numerical stability.

We compare the results simulated by the Maxwell-Schrödinger and Maxwell-Newton schemes for the following three electrostatic potentials V_h, V_{la}, and V_{ga} :

$$V_h = \frac{m\omega_h y^2}{2}, \tag{2.21}$$

$$V_{la} = V_h + V_l \exp\left\{-0.5\left(\frac{y_l + y}{\sigma_l}\right)\right\}, \tag{2.22}$$

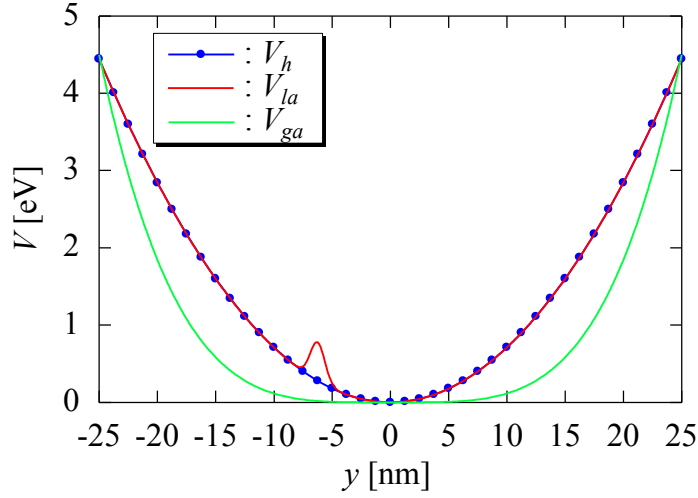$$V_{ga} = V_g\left(\frac{y}{y_g}\right)^4, \tag{2.23}$$

FIG. 2.3. Spatial profile of the studied electrostatic potentials: the blue line with circles represents the harmonic potential V_h while the red and green lines denote the locally anharmonic potential V_{la} and globally anharmonic potential V_{ga}, respectively.

where the parameters characterizing the potentials, ω_h, V_l, σ_l, y_l, V_g, and y_g, are given as 50 Trad/s, 0.5 eV, 0.625 nm, $10\sigma_l$ nm, 4.5 eV, and 25 nm, respectively. The potential energy curves for these three potentials are plotted in Figure 2.3. As displayed in this figure V_h is a single-well and harmonic potential, while V_{la} is almost identical to this V_h potential but is locally supplemented by a small anharmonic 'humps' located at around $y = -6.25$ nm. This hump allows the quantum electron to bifurcate every time when it impinges on the hump owing to tunnelling while does not for the classical electron. The third potential V_{ga} is a single-well but globally anharmonic potential, which allows us to investigate a different quantum mechanical effect other than that caused by tunnelling. We have chosen the ground state of each of these electrostatic potentials as the initial wave packet in all quantum simulations.

2.2.1 Excitation by a strong electromagnetic field

The time responses of the polarization current density **J** in the thin film obtained by the two hybrid simulations are represented in Figure 2.4, where the blue solid and red broken lines represent, respectively, the numerical results obtained by the Maxwell-Schrödinger and Maxwell-Newton schemes. Figure 2.4 (a) representing the results for the single and harmonic well V_h shows that both results agree excellently, indicating that the classical theory of the Maxwell-Newton scheme can be safely used for this case. On the other hand, Figure 2.4 (b), displaying the results for the locally anharmonic double-well potential V_{la}, shows that the polarization current densities obtained from these two schemes deviates from each other more and more strongly after the first

16

30 fs. This indicates that the Maxwell-Newton scheme is unreliable for this locally anharmonic potential. The results displayed in Figure 2.4 (c) for the single but globally anhamonic well V_{ga} shows a trend somewhat between (a) and (b): the polarization current density of the Maxwell-Newton scheme roughly follows that of the Maxwell-Schrödinger scheme, but there can be observed a quantitative difference between them. This indicates that the Maxwell-Newton scheme could become unreliable for quantitative calculation even when the confining potential is single but globally anharmonic well.
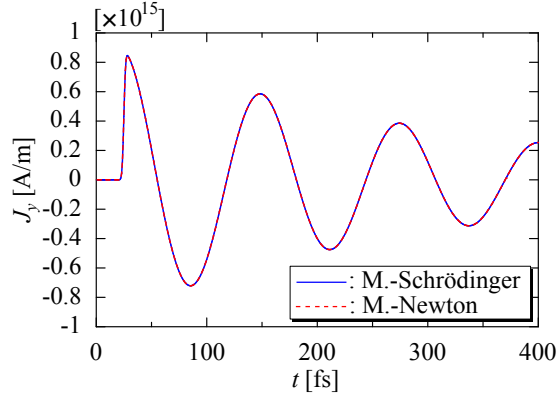
(a)
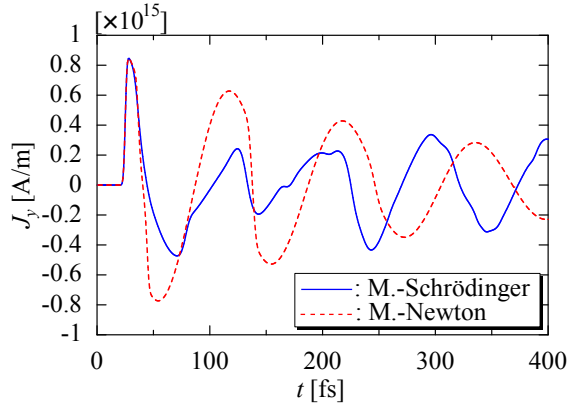
(b)
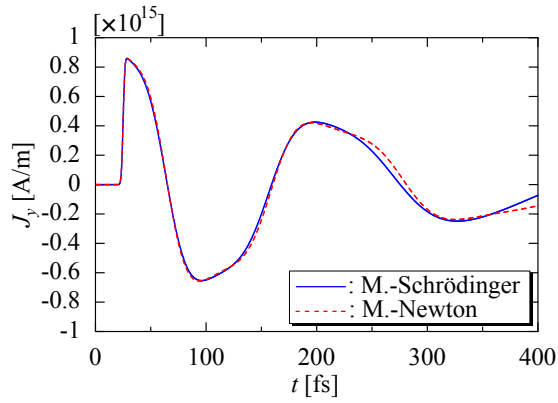
(c)

FIG. 2.4. Comparison of the time response of the polarization current density for the electrostatic potentials V_h, V_{la}, and V_{ga} (See Figure 2.3). (a), (b), and (c) correspond, respectively, to the case for the electrostatic potentials V_h, V_{la}, and V_{ga}. The blue solid and red broken lines represent the results obtained by the Maxwell-Schrödinger and Maxwell-Newton schemes, respectively.

In order to rationalize the observed trends, we have investigated the dynamics of electron in the thin film, namely, the spatiotemporal propagation of the electron wave packets and the corresponding classical trajectories obtained, respectively, by the Maxwell-Schrödinger and Maxwell-Newton schemes. The results for the three electrostatic potentials V_h, V_{la}, and V_{ga} are displayed in Figures 2.5 (a), (b), and (c), respectively. In the figures the thick oscillatory curve in color whose scale is displayed on the right end of each figure indicates the time-evolution of the probability density of the electron wave packet $|\psi|^2$ and the triangles plotted in the same figure denote the classical trajectory. On the left-hand side of each figure the potential energy curve of the corresponding electrostatic potential is also plotted. The vertical axes for both sides of the figure commonly indicate the y axis. As shown in Figure 2.5 (a) representing the results for the single and harmonic well V_h, the electron wave packet is localized at each time step keeping a Gaussian shape similar to the ground state and closely follows the corresponding classical trajectory. This excellent agreement between the quantum and classical electron dynamics results in an almost identical behaviour of the current densities obtained by these two schemes as displayed in Figure 2.4 (a). On the other hand, Figure 2.5 (b) representing the results for the double-well and locally anharmonic potential V_{la} shows that the electron wave packet gets fragmented into several pieces due to the tunnelling. Furthermore interference among these fragments makes the wave packet complicated even further. Since the classical dynamics could not support such fragmentation and interference, the current density obtained by the Maxwell-Newton scheme deviates largely from that obtained by the Maxwell-Schrödinger scheme as observed in Figure 2.4 (b). Figure 2.5 (c), representing the results for the globally anharmonic potential V_{ga}, shows that the electron wave packet follows the corresponding classical trajectory in the beginning before $t \sim 200$ fs. For the later time t, however, the electron wave packet starts to spread gradually and a nodal structure in the probability density appears. This nodal structure reflects the fact that the electron wave packet is no more a single Gaussian distribution but is fragmented into a few components. In case for purely harmonic electrostatic potentials an initial Gaussian wave packet remains to be a Gaussian through time propagation. Therefore, the observed fragmentation is caused by global anharmonicity in the electrostatic potential, which induces dephasing of the electron wave packet. Since classical mechanics cannot account for such dephasing effects, the classical trajectory deviates from the center of the electron wave packet, which causes a difference in the polarization current density between the two schemes.
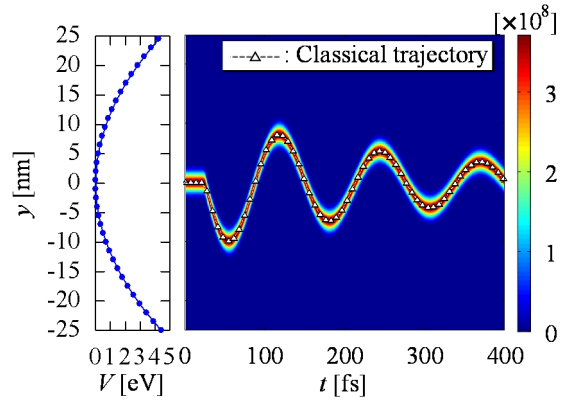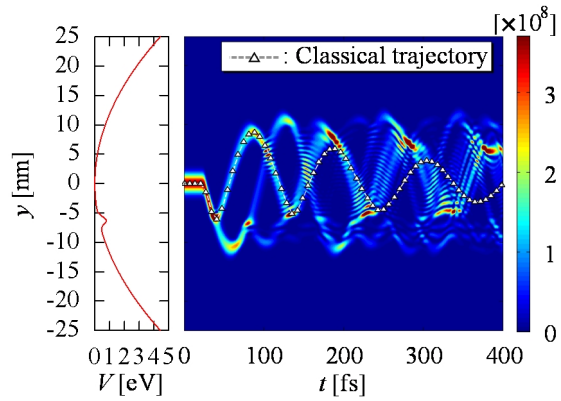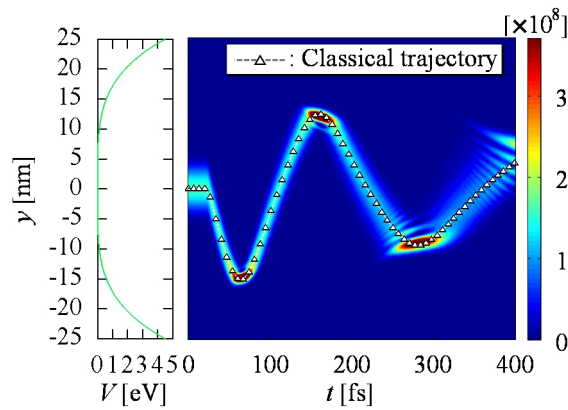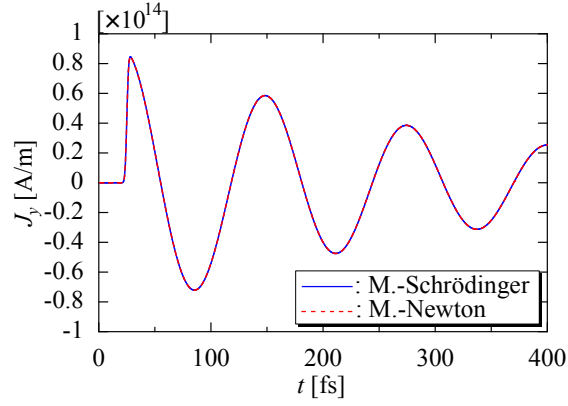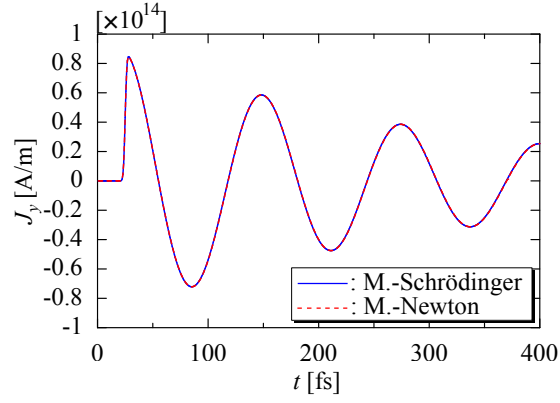
FIG. 2.5. Time evolution of the electron wave packet and the corresponding classical trajectory. (a), (b), and (c) indicate, respectively, the results for the electrostatic potential V_h, V_{la}, and V_{ga}. The spatial profile of the potential is displayed on the left-hand side of each figure. The thick curve in color scale represents the probability density of the electron.

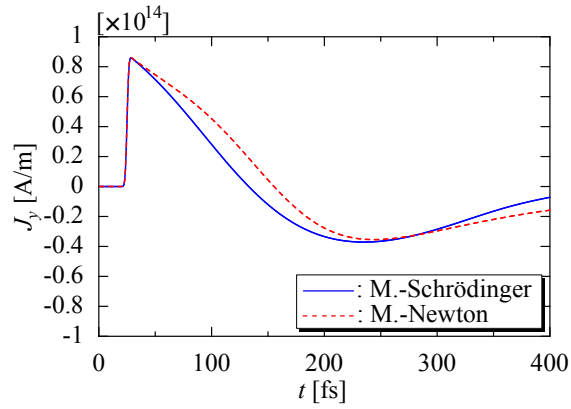## 2.2.2　Excitation by a weak electromagnetic field

Next, we have examined a dependence of the computational results on the strength of the applied laser field. Since the applied laser field we have studied so far is rather strong, we have employed a weaker laser field here by decreasing the amplitude of the current sources 10 times smaller than that used for the simulations in Figures 2.4 and 2.5 as $J_0 = 100$ MA/m. Figures 2.6 (a) and (b) display the resultant time responses of the polarization current densities **J** for the harmonic single- and locally anharmonic double-well potentials V_h and V_{la}. The blue solid and red broken lines represent the results obtained by the Maxwell-Schrödinger and Maxwell-Newton schemes, respectively, as for Figure 2.4. Unlike the results in Figure 2.4 the polarization current densities for not only the harmonic single-well potential V_h but also the locally anharmonic double-well potential V_{la} obtained by the two schemes agree very well as displayed in Figure 2.5 (a) and (b). On the other hand, Figure 2.6 (c) representing the result for the gobally anharmonic single-well potential V_{ga} shows that the computational results by the two hybrid simulations still differs quantitatively from each other.

(a)



(b)

(c)

FIG. 2.6. Comparison of the time response of the polarization current density for different electrostatic potentials. (a), (b), and (c) correspond, respectively, to the cases of V_h, V_{la}, and V_{ga}. The thin film is subjected to the weak electromagnetic fields excited by current sources with the amplitude $J_0 = 100$ MA/m. See the caption to Figure 2.4 for other remarks.
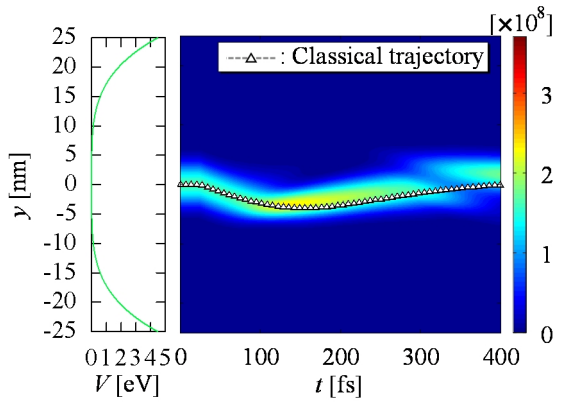
As has been done in Figure 2.5 for the strong electromagnetic field, the time evolution of the electron wave packet and the corresponding classical trajectory for this weak laser field are displayed in Figure 2.7, where (a), (b), and (c) denote the numerical results for V_h, V_{la}, and V_{ga}, respectively. It is noted that Figures 2.7 (a) and (b), representing the results for V_h and V_{la}, are almost identical to each other and that no fragmentation of the electron wave packet is observed for the locally anharmonic double-well case unlike the corresponding result in Figure 2.5 (b). This can be rationalized by the small strength of the laser field as follows: Since the electric field of the laser pulse is small, it could not give enough energy to the electron to reach the hump of the potential, namely local anharmonicity, for V_{la}. Therefore, since the potential energy curves of V_h and V_{la} below this hump are exactly the same harmonic potential, their electron dynamics should naturally be identical to each other for this weak strength of the laser field. In the case of the globally anharmonic potential V_{ga} illustrated in Figure 2.7 (c), however, the electron wave packet spreads as the time proceeds and it undergoes bifurcation after $t = 300$ fs. Therefore, this dephasing effect existing only in the quantum simulation causes a difference between the results obtained by the two schemes even when the laser field is sufficiently weak.
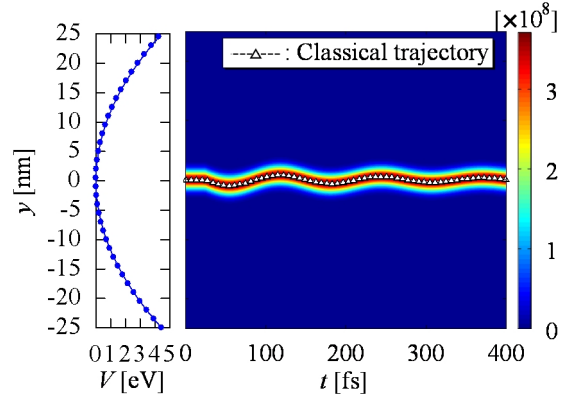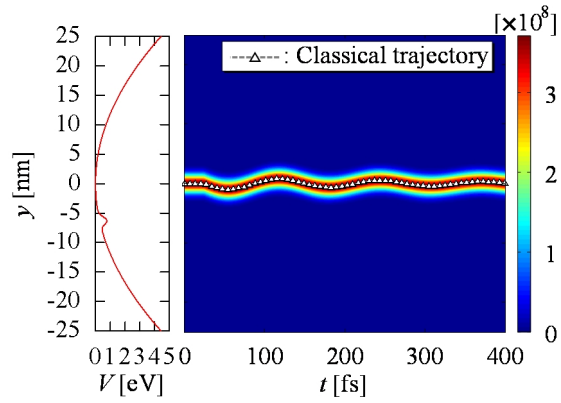
FIG. 2.7. Time evolution of the electron wave packet and the corresponding classical trajectory for the weak electromagnetic fields excited by current sources with the amplitude $J_0 = 100$ MA/m. (a), (b), and (c) correspond, respectively, to the cases of the electrostatic potential V_h , V_{la} , and V_{ga} . See the caption to Figure 2.5 for other remarks.

24

The present investigations show that the conventional Maxwell-Newton scheme can be applied not only to macroscopic problems as have been studied in most cases but also to microscopic problems of a nano-scale order on condition that the electrostatic confining potential for electron is purely harmonic. However, when the electrostatic potential deviates from a harmonic one even slightly, the Maxwell-Newton scheme would give unreliable results owing to quantum-mechanical tunnelling and/or anharmonicity effects. Therefore, such problems should be solved by the Maxwell-Schrödinger hybrid scheme.

2.3 Discussion

In this section we have focused on light-matter interaction by many electron systems especially with respect to the anharmonisity of the confining electrostatic potential, and investigated the interaction between laser fields and a nano-scale thin film, assumed as the surface of plasmonic devices, which is modelled by a representative electron among those. The two distinct hybrid simulations, the Maxwell-Schrödinger and the conventional Maxwell-Newton schemes, have been compared for three types of the potential structure consisted of the harmonic single-, locally anhharmonic double-, and globally anharmonic single-well. The computational results show that the two multi-physics simulations provide almost identical results for the harmonic confining potential, indicating a validity of use of the conventional Maxwell-Newton scheme for this case. In the case of the locally anharmonic double-well potential, however, the results by the Maxwell-Newton approach differ significantly from those by the Maxwell-Schrödinger approach when the tunnelling plays an important role. Finally, for the case of the globally anharmonic single-well potential, the result of the Maxwell-Newton simulation deviates from that of the Maxwell-Schrödinger simulation quantitatively owing to an effect of dephasing of the electron wave packet by the anharmonicity in the electrostatic potential. These results have clearly demonstrated that the Maxwell-Schrödinger scheme is indispensable to multi-physics simulation particularly when the tunnelling, interference and anharmonicity effects play an essential role.

3 Light-matter interaction: single-electron systems

A novel scheme of designing laser pulses for controlling discrete quantum states has been proposed relying on the highly-accurate Maxwell-Schrödinger hybrid simulation. A single electron confined in a quasi-one-dimensional nanoscale potential well has been used as an illustrative example and a control pulse to be modulated as transferring completely the probability density from the ground state to the first excited state has been designed by the present Maxwell-Schrödinger hybrid scheme and by the conventional one that solves the time-dependent Schrödinger equation only without accounting for feedback from the electron system to the external electromagnetic field. The resultant pulses obtained by these two methods can be different largely owing to the modification of the laser field by the locally strong radiation from the excited electron. The present study demonstrates that light control pulses designed by the conventional method may need to be rectified for practical implementation in experimentations.

3.1 Theoretical model and computational details

In the present study we consider a model system of an electron confined in a quasi-one-dimensional space (chosen as being parallel to the z axis) and irradiated by a pulsed laser field polarized along this z axis. The geometry and coordinates of the studied system is schematically illustrated in Figure 3.1. Since the laser field is polarized along the z axis, the initial electric and magnetic fields, $\mathbf{E}$ and $\mathbf{H}$, have only the z and y component, respectively, i.e., $\mathbf{E} = (0, 0, E_z)$ and $\mathbf{H} = (0, H_y, 0)$ as displayed in Figure 3.1. Also the other components of electromagnetic fields, however, must be solved because those explicitly appear as soon as near field by the excited electron is generated. Therefore, the model system simulated here has the three- and one-dimensional degree of freedom for the electromagnetic fields and electron, respectively. After this subsection the formulation of Maxwell-Schrödinger hybrid scheme to solve the 3D-1D problem will be described with conventional designing scheme for a light control pulse [32].
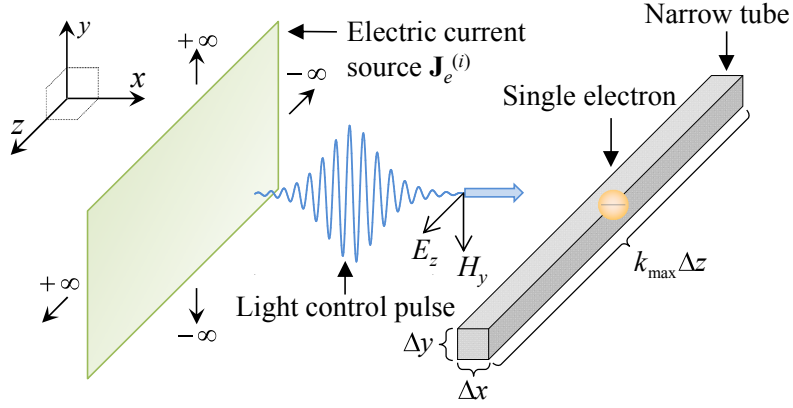
FIG. 3.1. The geometry and coordinates of the studied system. A single electron is confined in a rectangular narrow tube placed parallel to the z axis (right hand side of the figure) and it has a degree of freedom only along this axis. The electric current source $\mathbf{J}_e^{(i)}$ of the incident laser pulse is distributed uniformly on the y-z plane (left hand side of the figure) and excites a plane-wave light control pulse polarized along the z axis.

3.1.1 Maxwell-Schrödinger hybrid scheme for 3D-1D problems

The time-dependent wave function ψ of this non-relativistic electron confined in a quasi-one-dimensional potential V and subjected to a radiation field with its scalar potential φ and z component of the vector potential A_z is obtained by solving the following Schrödinger and Maxwell's equations,

$$i\hbar \frac{\partial \psi}{\partial t} = \left[\frac{1}{2m}\left(-i\hbar \frac{\partial}{\partial z} - qA_z \right)^2 + q\varphi + V \right]\psi, \tag{3.1}$$

$$\frac{\partial \mathbf{E}}{\partial t} = \frac{1}{\varepsilon_0}\nabla \times \mathbf{H} - \frac{1}{\varepsilon_0}\mathbf{J}, \tag{3.2}$$

$$\frac{\partial \mathbf{H}}{\partial t} = -\frac{1}{\mu_0}\nabla \times \mathbf{E}, \tag{3.3}$$

where $\mathbf{J} = (0, 0, J_z)$ represents the z component of the polarization current density. The vector and scalar potentials, $\mathbf{A}$ and φ, satisfy the following relations in the Lorentz gauge as

$$\frac{\partial \mathbf{A}}{\partial t} = -\mathbf{E} - \nabla \varphi, \tag{3.4}$$

$$\frac{\partial \varphi}{\partial t} = -\frac{1}{\mu_0 \varepsilon_0}\nabla \cdot \mathbf{A}. \tag{3.5}$$

The Lorentz gauge is employed here, since it is convenient for solving Maxwell's equations numerically in the sense that it automatically satisfies the causality relation for space and time

27

required by relativity.

Schrödinger equation [Eq. (3.1)] and Maxwell's equations [Eqs. (3.2) and (3.3)] are mutually coupled through φ and A_z in Eq. (3.1) and $\mathbf{J}$ in Eq. (3.2), respectively. The latter is defined by the time-dependent wave function ψ as

$$J_z = \frac{q\hbar}{2im}\left(\psi^*\frac{\partial\psi}{\partial z} - \psi\frac{\partial\psi^*}{\partial z}\right) - \frac{q^2}{m}|\psi|^2 A_z. \tag{3.6}$$

These equations (3.1) - (3.6) describe the following physical situation: An external laser field is propagating by Maxwell's equations (3.2) and (3.3) towards the confined electron system. When the laser field arrives, the electron starts to propagate by Schrödinger equation (3.1) under the influence of the scalar and vector potentials, φ and A_z, which have been updated by Eqs. (3.4) and (3.5). Then, the excited electron creates a polarization current density as defined by Eq. (3.6), which in turn goes into Eq. (3.2) of Maxwell's equations. This feedback from the excited electron to the electromagnetic field refines the laser field, which interacts again with the electron system and repeats the cycle mentioned above. Although the incident electromagnetic field is polarized along the z axis having thus only E_z and H_y components initially, it acquires other nonzero components through interacting with the electron. Therefore, all components of the electromagnetic field, namely E_x, E_y, E_z, H_x, H_y, H_z, as well as the vector and scalar potentials, A_x, A_y, A_z, and φ, need to be evaluated throughout the simulation.

3.1.2   Conventional pulse designing scheme

In the traditional theory of light-matter interaction in atomic and molecular physics the feedback from the electron systems to the electromagnetic field described in the last subsection has been neglected in most cases. The major reason for it may be a small number of charged particles included in an atom or a molecule in comparison to the huge number of photons in a laser pulse. Neglecting this feedback allows one to treat propagation of the electromagnetic field and electron separately. One can then focus only on the electron system and solves the time-dependent Schrödinger equation with the effect of electromagnetic field included as a pre-defined time-dependent potential. The scalar potential φ for the electromagnetic field is then chosen as being permanently zero (radiation gauge) independently from that for the electron system, which makes Eqs. (3.4) and (3.5) simpler as

$$\frac{\partial\mathbf{A}}{\partial t} = -\mathbf{E}, \tag{3.7}$$

$$\nabla\cdot\mathbf{A} = 0. \tag{3.8}$$

The potential function in the Schrödinger equation (3.1) then becomes only the electrostatic confining potential V. The effect of electromagnetic field on the electron thus appears only in the vector potential $\mathbf{A}$ in Eq. (3.1).

There are a number of known ways to transform the time-dependent Schrödinger equation of Eq. (3.1) to a particular form suitable for actual computation thanks to the gauge invariance of expectation values of observables under any unitary transformations. Among others, the so-called length gauge [41] is often used for atoms and molecules, since the dipole approximation, that is, neglecting the position dependence of the vector potential, such that $\mathbf{A}(\mathbf{r},t) \sim A(t)$, is valid for a typical wavelength of laser lights and since the transformed Hamiltonian becomes a simple sum of the field-free atomic or molecular Hamiltonian and a dipole interaction term in this representation, as shown below. We introduce a unitary transformation to perform a displacement of the wave function in a momentum space defined as

$$\hat{\tau} \equiv \exp[-iqA_z(t)z/\hbar].\tag{3.9}$$

By applying this unitary transformation to the wave function ψ on both sides of Eq. (3.1) and then rewriting the vector potential into the electric field by Eq. (3.7), the time-dependent Schrödinger equation for the transformed wave function $\widetilde{\psi} \equiv \hat{\tau}\psi$ becomes

$$i\hbar\frac{\partial\widetilde{\psi}}{\partial t} = \left[-\frac{\hbar^2}{2m}\frac{\partial^2}{\partial z^2} - qE_z(t)z + V\right]\widetilde{\psi}.\tag{3.10}$$

We use this length gauge form of the time-dependent Schrödinger equation in the next section for obtaining a light control pulse in the conventional method.

3.1.3   FDTD method, electrostatic confining potential, and space-time grids

The time propagation of the electromagnetic field and the electron wave packet described by Eqs. (3.1) - (3.6) and (3.10) in the previous subsections 3.1.1 and 3.1.2 is performed by the FDTD method [14-16, 18-19, 36-39], where the mathematical formulas for practical use in coding are described in detail in Appendix. The electromagnetic field and the wave function are thus discretized and represented on the common space-time grid points explained in detail below.

The electrostatic confining potential V is chosen as a simple bowl like potential defined by

$$V = V_0\left(\frac{z}{z_{\max}}\right)^4,\tag{3.11}$$

where the parameters V_0 and $z_{\max}$ characterizing the potential are set as 5000 eV and 1.0 nm, respectively. This kind of a bowl-like potential simulates the confining potential of quantum dots or nanowires [42-44]. The spatial profile of this electrostatic potential as well as the wave functions of the ground state and of the first excited state, ψ_0 and ψ_1, for an electron confined in this potential are displayed in Figure 3.2. The energy difference between these two states is 5.3 eV. In the present study we have focused on these two states and studied light control pulses that
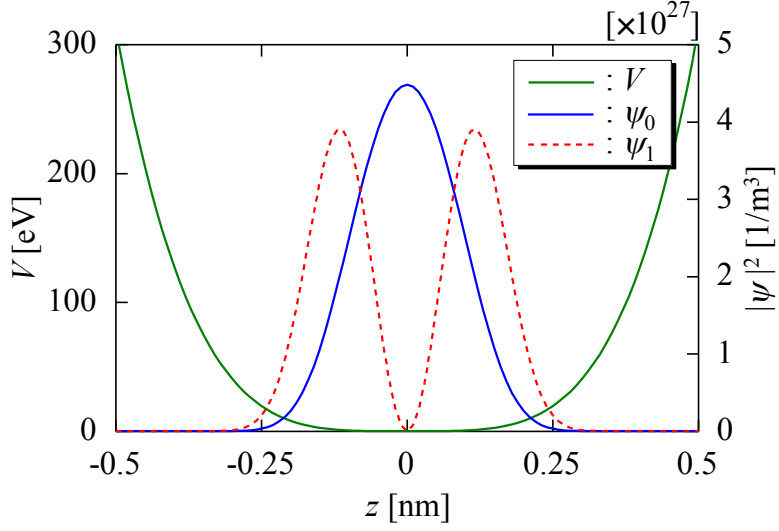
FIG. 3.2. Spatial profile of the studied electrostatic potential V (in eV) and the probability density distributions of the ground ψ_0 state (solid blue line) and of the first excited ψ_1 state (broken red line). The eigenenergies of the ground and first-excited states are 2.05 and 7.35 eV, respectively.

transform the ground state into the first excited state.

The space- and time-grids have been generated as follows. The grid is equispaced and its spacing for the x and y coordinates, Δx and Δy, has been both set as 1.0 nm while it has been set as 0.01 nm for the z coordinate, Δz. The number of grid points i_{max} and j_{max} for x and y coordinates have been set as 40 while it has been set as 201 for z-coordinate, k_{max}. The origin of the space coordinate system coincides with the centre of the electrostatic potential. The spacing for the time grid Δt is not independent from the spacings for the space grid, Δx, Δy, and Δz but has to be chosen so as to satisfy Courant-Friedrichs-Lewy (CFL) condition [37]. In order to guarantee numerical accuracy the time spacing Δt has been chosen in the present study to be smaller by a factor of 0.9 than the maximum value allowed by the CFL condition.

The normalization of the wave function is as follows. Since the electron is confined in the quasi-one-dimensional space extending along the z axis like a "tube", its wave function is dependent only on the z coordinate. Along the x and y coordinates the wave function is assumed to be uniform and has a nonzero value only within one unit Δx and Δy of the grid cell. Therefore, its probability density is zero outside of this narrow tube. The wave function ψ of the electron is thus normalized as

$$\Delta x \Delta y \int_{-\infty}^{\infty} |\psi(z)|^2 \, dz = 1. \tag{3.12}$$

3.2 Computational results

3.2.1 Conventional light control pulse

In this section we investigate the efficiency of light control pulses obtained by the conventional method, i.e., neglecting feedback from the electron system to the electromagnetic fields. The Maxwell-Schrödinger hybrid simulation described in the previous section is employed to study the near field generated by the interaction between the laser field and electron as shown in Figure 3.1. Among several variants of the conventional method in designing light control pulses we have focused on the method developed by Ohtsuki *et al.* [32], which is very simple but efficient. The light control pulse in the conventional method has been obtained as follows. Firstly, we set the initial state $\widetilde{\psi}(z, t = 0)$ and the target or objective state ψ_ξ. These states are basically the ground state and the first excited state, ψ_0 and ψ_1, respectively, as mentioned in the previous section, but for a convenience of computational convergence, the following initial state that incorporates a very tiny amount of the target state has been used as

$$\widetilde{\psi}(z, t = 0) = \sqrt{0.9999}\psi_0 + \sqrt{0.0001}\psi_1. \tag{3.13}$$

This condition is used only for generating a light control pulse. Time-dependent simulations with an optimized light control pulse are done starting from the pure ground state without a contamination of the target state.

A control pulse is usually designed so as to maximize the probability density of the objective state within a certain time duration. Therefore, the following cutoff function has been used to force the strength of the laser pulse decaying exponentially after a given time τ as

$$E_0 = \eta \exp\left\{-\frac{t - t_0}{\gamma}u(t - t_0)\right\}, \tag{3.14}$$

where η, t_0, and γ have been chosen as 0.5 GV/m, 15 fs, and 3 fs, respectively, with $u(t)$ denoting the unit step function. Following the study by Ohtsuki *et al.*, the conventional pulse $E_z^{(i)}(t)$ has been constructed here by solving the equation,

$$E_z^{(i)} = -2\frac{E_0}{m}\text{Im}\langle\widetilde{\psi}|Wqz|\widetilde{\psi}\rangle, \tag{3.15}$$

where W denotes the projection operator to the objective state, namely,

$$W = |\psi_\varsigma\rangle\langle\psi_\varsigma|. \tag{3.16}$$

Eq. (3.15) can be derived by a more general formulation based on the optimal control theory [30-31]. Briefly, the light control pulse $E_z^{(i)}(t)$ is constructed so as to take an extremal value in the following objective functional $I[E_z^{(i)}(t)]$, defined by the sum of a functional K to maximize the expectation value of the target operator W at a controlling time t_f and a penalty function to avoid
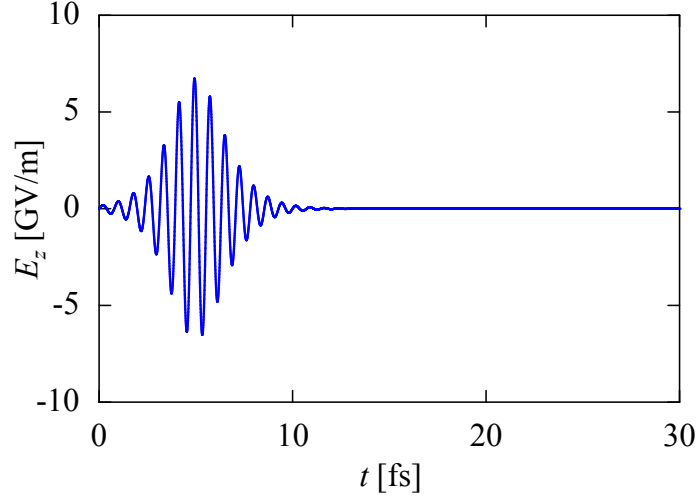
FIG. 3.3. Temporal profile of the light control pulse $E_z^{(i)}$ obtained by the conventional method. This pulse is designed to transfer the probability density of an electron confined in the electrostatic potential V [See Eq. (3.11)] from the ground state to the first excited state (See also Figure 3.2).

a too high intensity of the laser pulse, as

$$I\left[E_z^{(i)}(t)\right] = K\left[\left\langle W(t_f) \right\rangle\right] - \int_{t_0}^{t_f} \frac{1}{\hbar G(t)} \left[E_z^{(i)}(t)\right]^2 dt. \tag{3.17}$$

The function $G(t)$ in the penalty function in second term of the right-hand side of the equation represents an arbitrary time-dependent weight. By setting $G(t) = 1$ and the functional K to be identity as a simplest choice, Eq. (3.17) together with the time-dependent Schrödinger equation (3.10) yields the equation (3.15) of determining the light control pulse. A low-pass filter has been also used after designing the light control pulse to clean numerical artifacts associated with an extremely high frequency over several thousand times higher than the transition angular frequency of 5.30 eV/$\hbar$. These numerical errors, although they are very tiny, are caused by the FDTD algorithm. The temporal profile of the resultant light control pulse $E_z^{(i)}$ designed by this method is displayed in Figure 3.3.

In order to implement this light control pulse in the Maxwell-Schrödinger hybrid simulation we employ the following incident electric current source $\mathbf{J}^{(i)}$ which is uniform on the x-y plane as shown in Figure 3.1:

$$\mathbf{J}^{(i)} = -\frac{2}{\Delta x Z_0} E_z^{(i)} \mathbf{a}_z, \tag{3.18}$$

where Z_0 represents the characteristic impedance in vacuum. This source generates a plane-wave pulse which propagates in the positive and negative x direction. In addition the following initial condition is employed in the hybrid simulation:

$$\psi(z, t = 0) = \psi_0. \tag{3.19}$$

32

3.2.2　Near field generated by a single electron

The spatiotemporal propagation of the z component of the electric field E_z, polarization current density J_z, and the probability density of the electron wave packet $|\psi|^2$ in the narrow tube obtained by the Maxwell-Schrödinger hybrid simulation employing the conventional light control pulse $E_z^{(i)}$ has been calculated and is displayed in Figure 3.4. The probability density distribution of the wave packet displayed in Figure 3.4 (c) shows a single-peak at the beginning of the time propagation reflecting the distribution of the ground state. It undergoes a drastic change at around $t = 3 \sim 4$ fs and becomes a double-peak distribution and stabilized after $t > 5$ fs. At the right end of Figure 3.4 (c) the probability density distribution of the objective state is displayed. The electron wave packet should become closer and closer to this distribution when the 'true' light control pulse is employed. Although it has undergone a transition as mentioned from a single-peak into a double-peak that reflects a node of the first excited state, it never becomes identical to the distribution of the objective state after the laser pulse has disappeared.
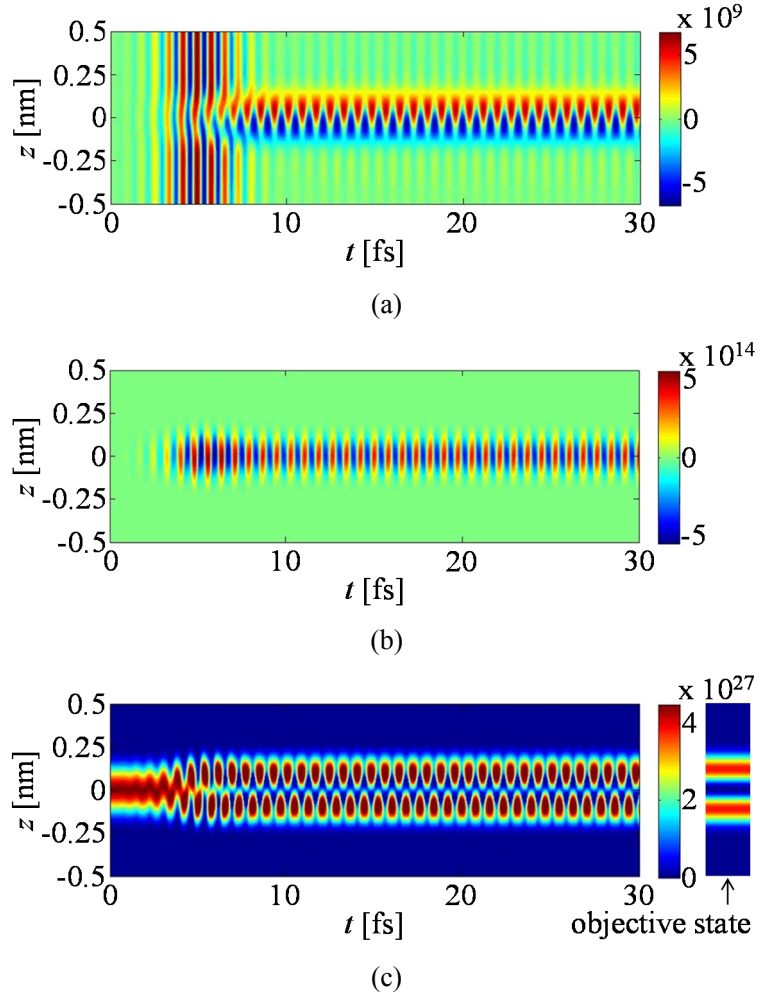
FIG. 3.4. The spatiotemporal propagation of the z component of the electric field E_z [(a)], the polarization current density J_z [(b)], and the probability density of the electron wave packet $|\psi|^2$ [(c)] obtained by the Maxwell-Schrödinger hybrid simulation employing the conventional light control pulse $E_z^{(i)}$. The size of the cross section of the tube (See Figure 3.1) is set as $\Delta x = \Delta y = 1.0$ nm. In all figures the horizontal and vertical axes represent the time t (in fs) and the z coordinate (in nm) in the narrow tube where the electron is confined. At the far right-end of the figure (c) the probability density distribution of the objective state is indicated.
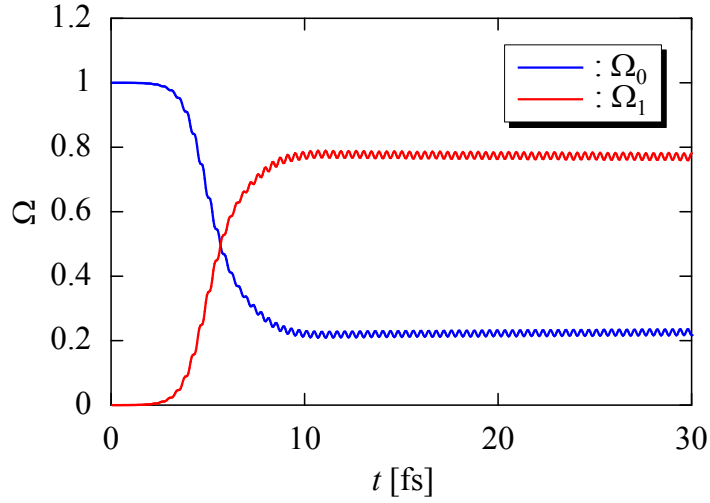
FIG. 3.5. The temporal variation of each component of the electronic states in the time-dependent electron wave packet obtained by the Maxwell-Schrödinger hybrid simulation employing the conventional light control pulse $E_z^{(i)}$. The size of the cross section of the tube (See Figure 3.1) is set as $\Delta x = \Delta y = 1.0$ nm. The blue and red lines represent the magnitude of the component of the ground state Ω_0 and of the objective state Ω_1, respectively [See Eqs. (3.20) and (3.21)].

A quantitative measure of the control ability of this conventional light control pulse has been estimated by projecting the time-dependent wave packet onto the ground ψ_0 state and the objective ψ_1 state, respectively, as

$$\Omega_0 = \langle \widetilde{\psi}' | \psi_0 \rangle \langle \psi_0 | \widetilde{\psi}' \rangle, \tag{3.20}$$

$$\Omega_1 = \langle \widetilde{\psi}' | \psi_1 \rangle \langle \psi_1 | \widetilde{\psi}' \rangle, \tag{3.21}$$

where we have applied the unitary transformation $\hat{\tau}$ to the time-dependent wave function ψ, such as $\widetilde{\psi}' \equiv \hat{\tau}\psi$, in order to evaluate the overlap of wave functions in the same gauge. The resultant time variation of Ω_0 and Ω_1 are displayed in Figure 3.5. Ω_0 and Ω_1 start from unity and naught, respectively, since the initial wave packet is prepared as the ground Ω_0 state. When the laser pulse is on, Ω_1 increases rapidly during the period of time $2 < t < 10$ fs in accord with the decrease of Ω_0, indicating that the component of the objective state in the time-dependent wave packet increases. However, Ω_0 and Ω_1 stay at around 0.25 and 0.75, respectively, even after the pulse has disappeared.

The origin of the observed insufficient control ability of the conventional light control pulse can be found in the time-propagation of the electric field and of the polarization current density displayed in Figures 3.4 (a) and 3.4 (b), respectively. The z component of the electric field E_z inside the tube is very low at the beginning of the laser pulse and becomes strong at around $t \sim 5$ fs when the peak of the laser pulse arrives as displayed in Figure 3.4 (a). We note here that the spatial dependence of the electric field on the z axis becomes appreciable almost at the same time

35

of the peak arrival. For example, at the time of $t \sim 5$ fs, the electric field in the "center" region of the tube ranging $|z| < 0.15$ becomes significantly weaker than in the rest part of the "outer" region of $|z| > 0.15$. This center region coincides with the region where the electron wave packet has a meaningful probability density. As the time proceeds further so that the intensity of the laser pulse becomes decreasing, the intensity of E_z in the outer region in turn decays rapidly while that in the center region around the vicinity of the wave packet persists or becomes even stronger.

This behavior of E_z is caused by the induced emission from the excited electron as confirmed by the result of the polarization current density displayed in Figure 3.4 (b). The polarization current density is very small at the beginning of the laser pulse since the electron is not excited enough remaining thus almost in the ground state. As the laser pulse rises, the electron is forced to move back and forth by the electric field of the laser pulse to acquire energy for reaching the objective state, that generates a strong polarization current in the center region as seen in the result at $t \sim 5$ fs in Figure 3.4 (b). This strong polarization of electron causes the weakening of the electric field around the center region of the tube. In the meantime after the laser pulse has gone, the electron is still in a mixed state between the ground and excited states, allowing the polarization current persisting as seen in the result of Figure 3.4 (b) for $t > 10$ fs. This polarization current creates a near field with an oscillatory electric field as confirmed by Figure 3.4 (a). The oscillation of the electric field then causes a small modification of the electron wave packet, which manifests itself with the small oscillations in the amplitude of Ω_0 and Ω_1 as observed in Figure 3.5 for $t > 10$ fs. This small oscillatory behavior of Ω_0 and Ω_1 can be seen only when the feedback from the electron system to the electromagnetic field is taken into account in the simulation as has been done in the present study. Eventually, the polarization current should diminish to zero owing to spontaneous emission but it occurs in a much longer time scale than in the present simulation.

In order to confirm our reasoning, namely that the excited electron disturbs the original light control pulse significantly, thus preventing an intended control of the system, we have varied the strength of the induced emission from the excited electron to see how it affects the control ability of the conventional light control pulse. This variation of the strength of the induced radiation can be achieved by changing the size of the cross section of the tube in which the electron resides, i.e., $\Delta x \Delta y$. As indicated by the normalization condition of the electron wave function in Eq. (3.12) the electron density can be increased or decreased by choosing a smaller or larger value of $\Delta x \Delta y$, respectively. In the case of the result displayed in Figure 3.4 we have chosen $\Delta x = \Delta y = 1.0$ nm. Therefore, we have performed similar simulation by choosing $\Delta x = \Delta y = 0.5$ nm and $\Delta x = \Delta y = 1.5$ nm. The results are displayed in Figures 3.6 and 3.7, respectively, in a similar manner as has been done for Figure 3.4.
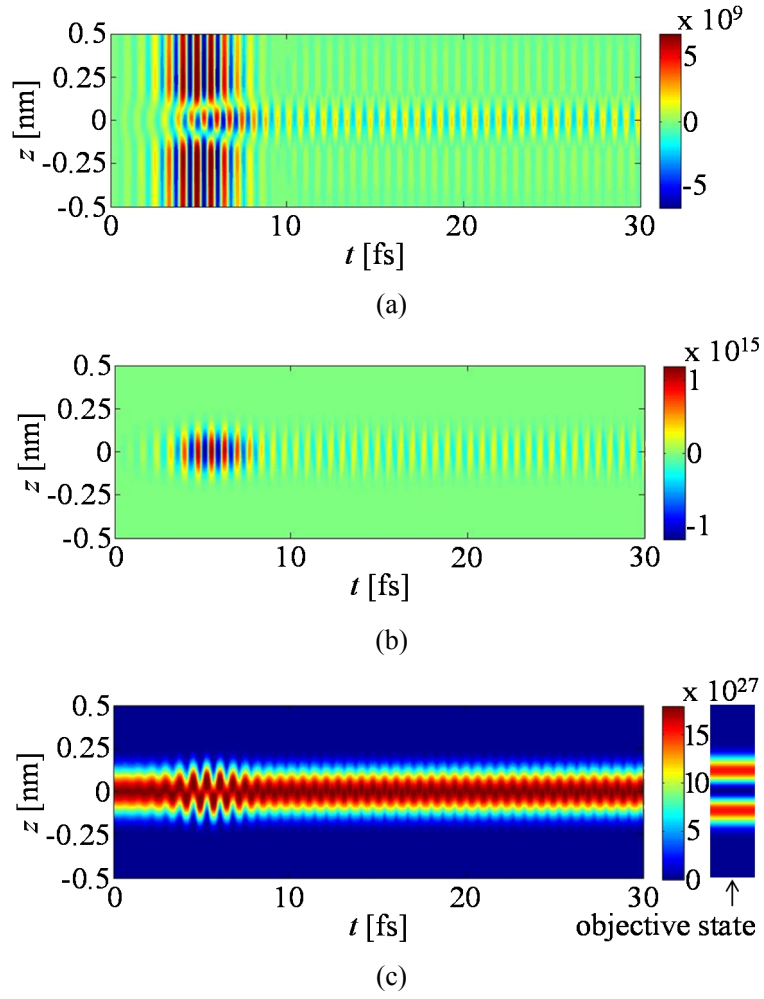
(a)

(b)

(c)

FIG. 3.6. The spatiotemporal propagation of the z component of the electric field E_z [(a)], the polarization current density J_z [(b)], and the probability density of the electron wave packet $|\psi|^2$ [(c)] obtained by the Maxwell-Schrödinger hybrid simulation employing the conventional light control pulse $E_z^{(i)}$. The size of the cross section of the tube (See Figure 3.1) is set as $\Delta x = \Delta y = 0.5$ nm. See the caption to Figure 3.4 for further details.
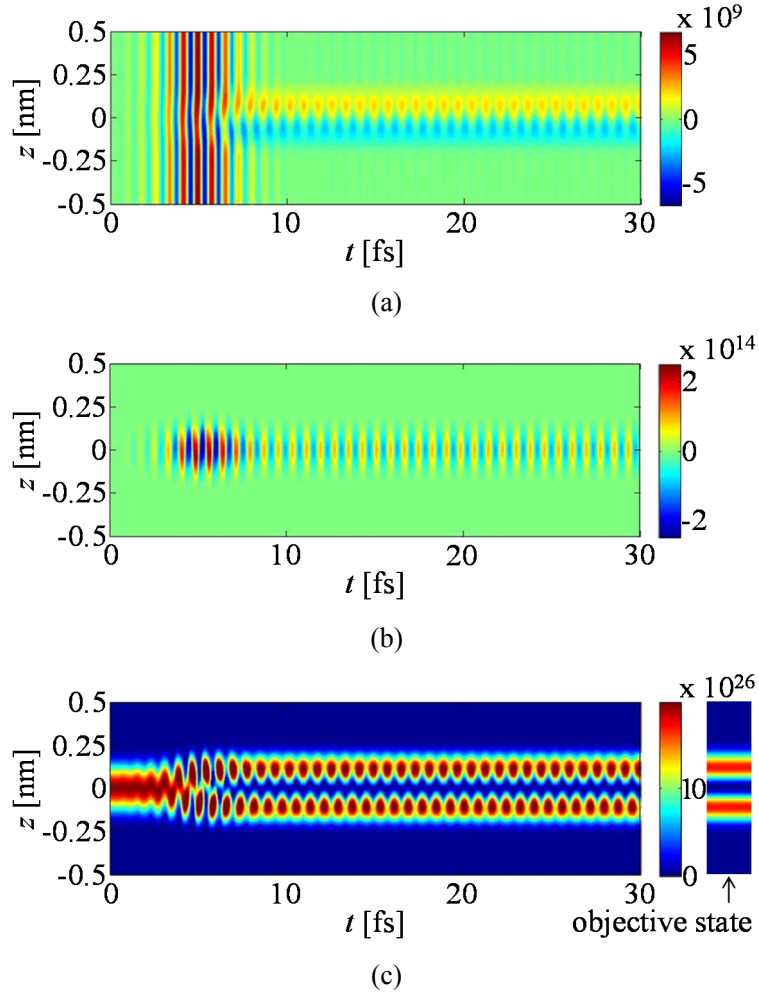
FIG. 3.7. The spatiotemporal propagation of the z component of the electric field E_z [(a)], the polarization current density J_z [(b)], and the probability density of the electron wave packet $|\psi|^2$ [(c)] obtained by the Maxwell-Schrödinger hybrid simulation employing the conventional light control pulse $E_z^{(i)}$. The size of the cross section of the tube (See Figure 3.1) is set as $\Delta x = \Delta y = 1.5$ nm. See the caption to Figure 3.4 for further details.

The results displayed in Figure 3.6 for the smaller value of Δx and Δy correspond to the case with a larger effect of the induced radiation. This is confirmed by the larger disturbance of the electric field E_z of the original laser pulse at around $t \sim 5$ fs as displayed in Figure 3.6 (a). Furthermore, the corresponding time-propagation of the electron wave packet displayed in Figure 6 (c) shows that the probability density along the z axis never becomes a double peak characteristic of the node structure of the wave function of the objective state. This indicates a lower control ability of the conventional light control pulse than in the case of $\Delta x = \Delta y = 1.0$ nm displayed in Figure 3.4. On the other hand, the results displayed in Figure 3.7 (c) corresponding to the case of $\Delta x = \Delta y = 1.5$ nm show that the probability density distribution along the z axis manifests itself a more clear doubly-peaked structure whose peak positions are closer to those of the objective state than does the case of $\Delta x = \Delta y = 1.0$ nm. This indicates a higher control ability of the conventional light control pulse in this case. We note here that in this case of a higher control ability the electric field E_z of the original light control pulse is less disturbed as confirmed by Fig. 3.7 (a).

In order to see a global trend of the control ability of the conventional pulse with respect to the size of the tube we have extended our simulation for different values of Δx and Δy ranging from 0.5 nm to 5.0 nm. The square of the projection of the wave packet obtained by the simulation onto the objective state, Ω_1, evaluated at $t = 30$ fs are summarized in Figure 3.8 for different values of Δx ($= \Delta y$). This figure shows that Ω_1 becomes larger and converges to unity in proportion to the increasing size of the cross section of the tube. This indicates that the conventional light control pulse can fully control the system in the limit of low density of electron. On the other hand, in case of smaller size of the tube than the case with $\Delta x = \Delta y = 2.0$ nm, the deviation of Ω_1 from unity becomes increasingly larger, indicating that the system can hardly be controlled by the conventional light control pulse.
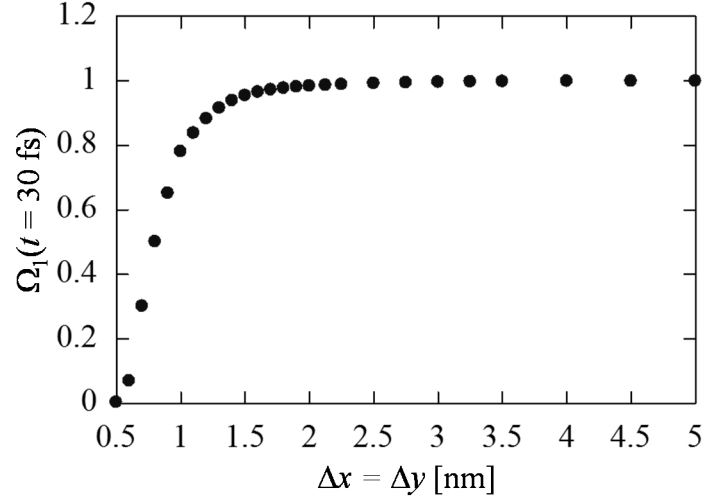
FIG. 3.8. The square-norm of the projection of the electron wave packet onto the objective state Ω_1 evaluated at $t = 30$ fs for the Maxwell-Schrödinger hybrid simulation employing the conventional light control pulse $E_z^{(i)}$. The horizontal axis represents the size of the cross section of the narrow tube (See Figure 3.1).

3.2.3   New light control pulse and its control ability

The last subsection 3.2.2 has clearly demonstrated that the conventional light control pulse designed without accounting for the near field generated by the excited electron could hardly control the system particularly when the charge density of the system is high. In this subsection we propose a novel scheme of designing light control pulses that takes into account the local modification of the incident laser field by the electron. The new scheme of designing light control pulses is a direct extension of the conventional method, i.e., to maximize the objective function under the constraint of avoiding too high laser intensity as described in Eq. (3.15), but it incorporates the effect of the modification of the incoming laser field. This can be done simply by replacing the time-dependent electron wave packet $\widetilde{\psi}$ in Eq. (3.15) obtained by the conventional method with the new one $\widetilde{\psi}'$, obtained by the Maxwell-Schrödinger hybrid simulation being transformed by a similar unitary transformation that is used to define the length gauge:

$$E_z^{(in)} = -2\frac{E_0}{m}\text{Im}\langle\widetilde{\psi}'|Wqz|\widetilde{\psi}'\rangle, \tag{3.22}$$

where a letter "n" is added to the superscript of the left-hand side of the equation as $E_z^{(in)}$ in order to discriminate it from the conventional pulse of $E_z^{(i)}$. The unitary transformation that transforms into ψ is similar to $\widetilde{\psi}'$ as mentioned above, but, unlike Eq. (3.9), the dipole approximation is not used here, namely,

$$\widetilde{\psi}' = \exp\left(-i\frac{q}{\hbar}A_z(z,t)z\right)\psi. \tag{3.23}$$

The control ability of the new light control pulse obtained by solving Eq. (3.22) has been examined by applying it to the same problem as described in the previous section 3.2.2. The resultant new light control pulse $E_z^{(in)}$ is displayed in Figure 3.9 for the case of $\Delta x = \Delta y = 1.0$ nm in both the time- and frequency-domain. In the frequency-domain spectrum the horizontal axis is normalized by the transition frequency. In the same figure the conventional light control pulse is also plotted as a reference. We have used the same parameters as have been used to design the conventional light control pulse $E_z^{(i)}$. This figure shows that there can be observed some meaningful difference in the amplitude and in the central frequency between the new and conventional light control pulses.
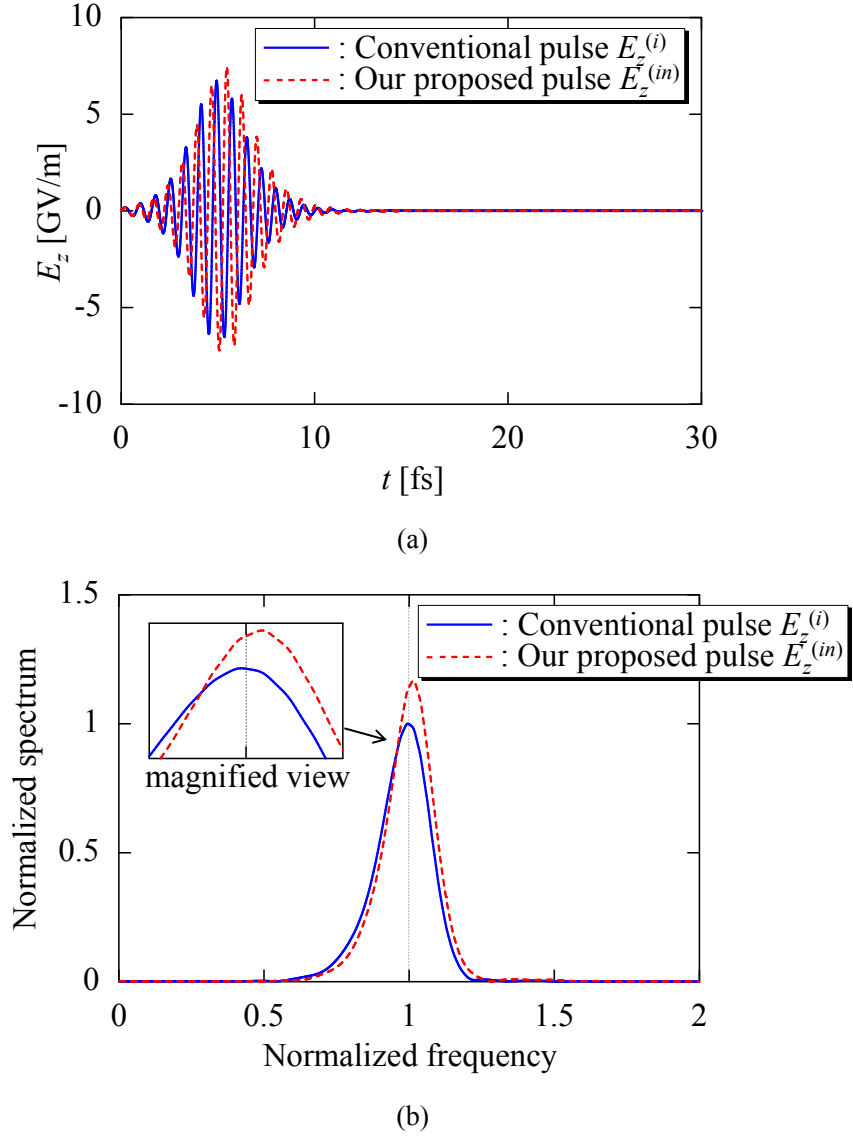
(a)

(b)

FIG. 3.9. A comparison between the light control pulses, $E_z^{(i)}$ and $E_z^{(in)}$, designed, respectively, by the conventional and the present Maxwell-Schrödinger hybrid simulation for the size of the cross section of the tube $\Delta x = \Delta y = 1.0$ nm: (a) and (b) represent the temporal profile of these pulses and their spectrum in the frequency domain. The blue solid and red broken lines represent $E_z^{(i)}$ and $E_z^{(in)}$, respectively. The horizontal axis of the figure (b) is normalized with respect to the transition frequency.

The time propagation of the electric field E_z, the polarization current density J_z, and the electron wave packet $|\psi|^2$ in the tube is displayed in Figure 3.10 as has been done for the case of Figures 3.4, 3.6, and 3.7. As displayed in Figure 3.10 (a) the incoming light control pulse interferes with the radiation field from the excited electron particularly at around $t = 5 \sim 10$ fs when the light intensity is strong. Further, during this period of time, the interfered pulse makes the electronic state stably reach the objective state as confirmed by Figure 3.10 (c). We note here that the z-component of the electric field remains as a static one even after the laser pulse has gone through the electron as displayed in Figure 3.10 (a) for $t > 10$ fs. This remaining static field is generated by the polarization charge density of the electron in its first excited state.
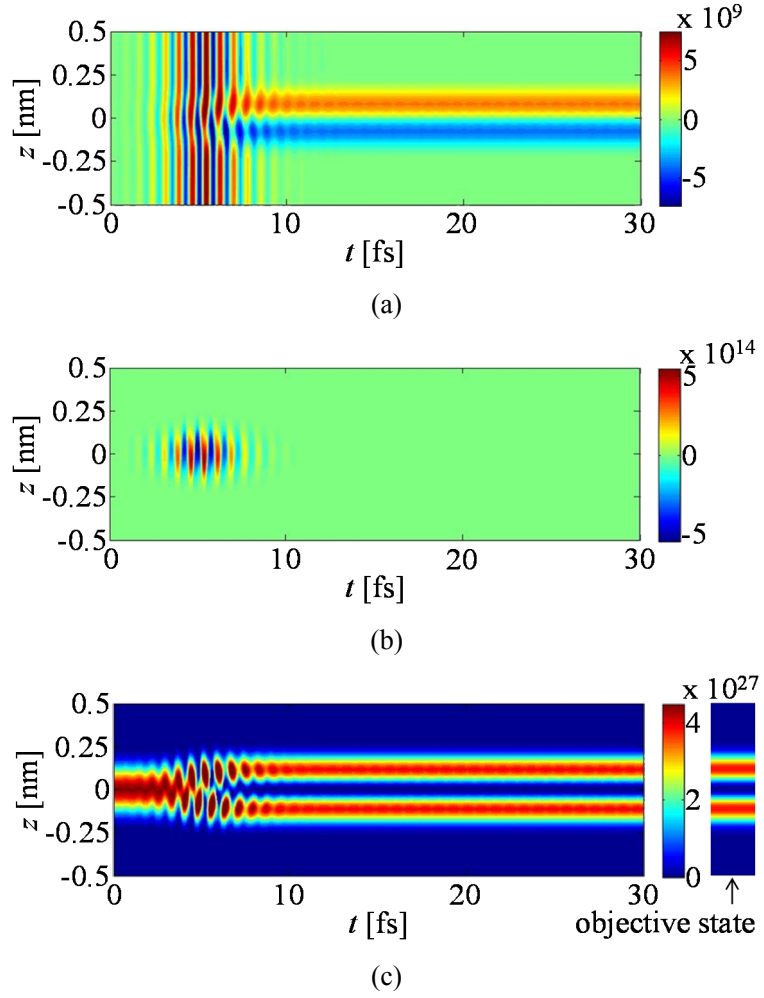
(a)

(b)

(c)

FIG. 3.10. The spatiotemporal propagation of the z component of the electric field E_z [(a)], the polarization current density J_z [(b)], and the probability density of the electron wave packet $|\psi|^2$ [(c)] obtained by the Maxwell-Schrödinger hybrid simulation employing the new light control pulse $E_z^{(in)}$. The size of the cross section of the tube (See Figure 3.1) is set as $\Delta x = \Delta y = 1.0$ nm. See the caption to Figure 3.4 for further details.

1.2

1

0.8

Ω 0.6

0.4

0.2

0

0   10   20   30

t [fs]
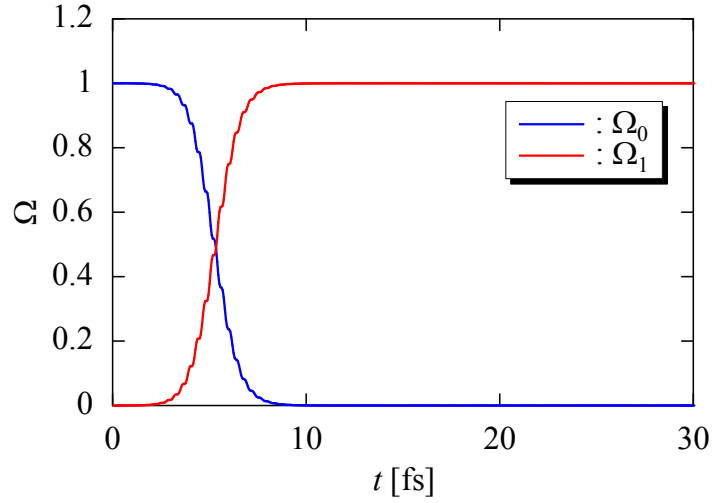
: Ω_0
: Ω_1

FIG. 3.11. The temporal variation of each component of the electronic states in the time-dependent electron wave packet obtained by the Maxwell-Schrödinger hybrid simulation employing the present new light control pulse $E_z^{(in)}$. See the caption to Figure 3.5 for further details.

The temporal variation of the probability density in the ground and objective states, Ω_0 and Ω_1, is displayed in Figure 3.11. Unlike the case for the conventional light control pulse displayed in Figure 3.5, the probability density in the objective state Ω_1 increases rapidly from zero to unity during the period of time $t = 3 \sim 10$ fs and is stabilized after the laser pulse has gone. These results indicate that the present new light control pulse can successfully control the quantum states by accounting for the modification of the incoming laser pulse by the excited electron.

Finally, in order to further confirm the reliability of the present method for designing light control pulses, the hybrid simulation with the new light control pulses has been performed for different sizes of the cross section of the tube, as has been done in the previous section 3.2.2. We have examined the cases with $\Delta x = \Delta y = 0.5 \sim 5.0$ nm, and in all cases the electron wave packet becomes the objective state after $t = 30$ fs within numerical accuracy.

As a demonstration, the resultant light control pulses for $\Delta x = \Delta y = 0.5$ and $\Delta x = \Delta y = 1.5$ nm are displayed in Figures 3.12 and 3.13, respectively. The conventional light control pulse is also displayed in the same figures for a comparison. Figure 3.13 representing the case with a small electron density shows that the light control pulse is rather similar to the conventional pulse. This is due to the fact that the induced radiation from the electron is weak. Therefore, the system can be somehow controlled by the conventional pulse. On the other hand, for the case with a high electron density the present light control pulse shows a large deviation from the conventional pulse as displayed in Figure 3.12. Since a larger electron density creates a stronger radiation, the electromagnetic field near the electron is modified more strongly, thus making the conventional pulse more and more impractical.
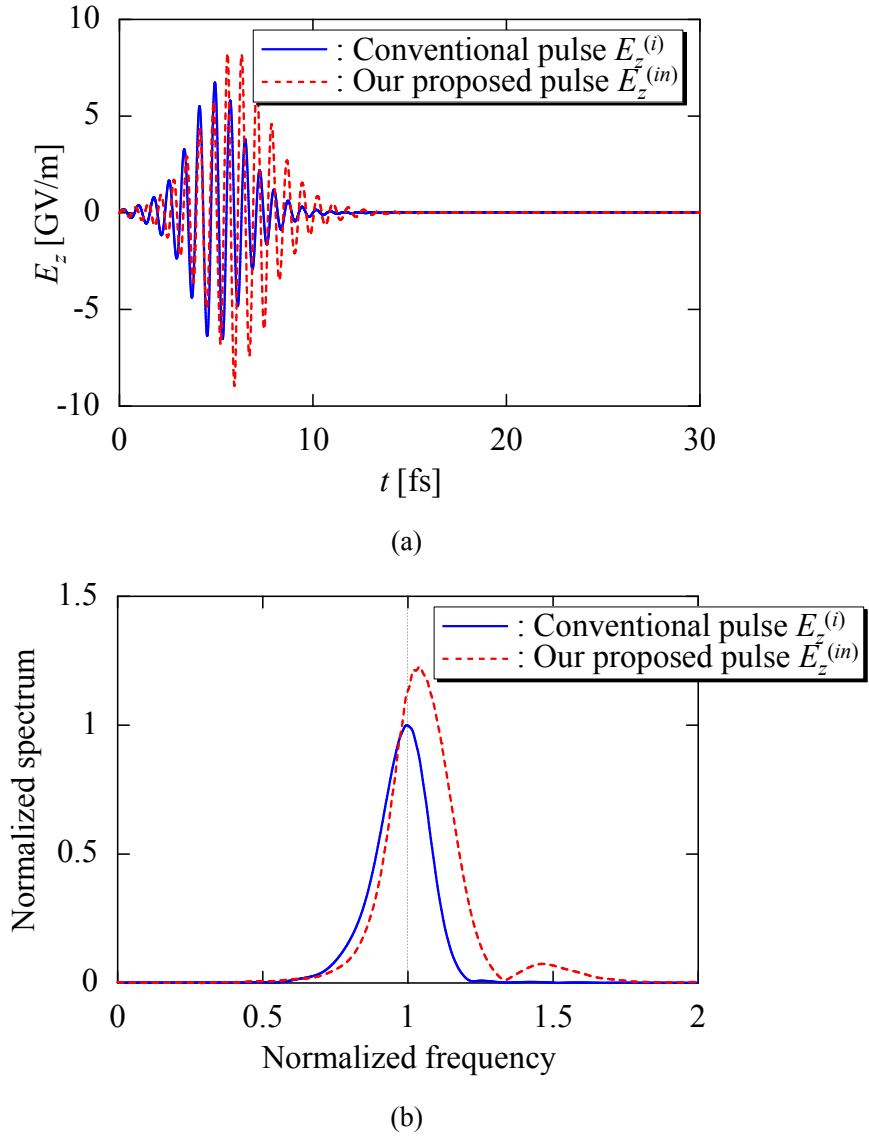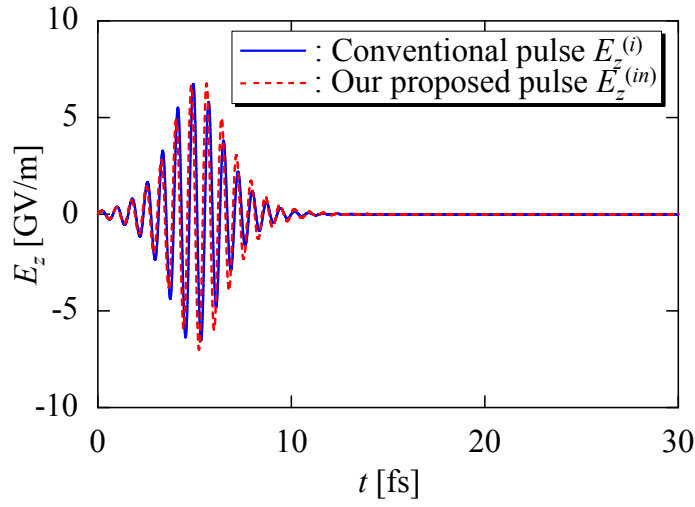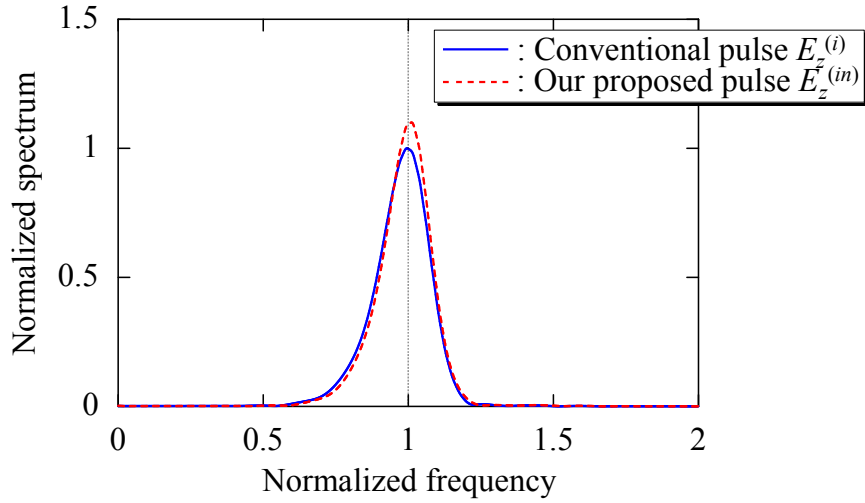
(a)

(b)

FIG. 3.12. A comparison between the light control pulses, $E_z^{(i)}$ and $E_z^{(in)}$, designed, respectively, by the conventional and the present Maxwell-Schrödinger hybrid simulation for the size of the cross section of the tube $\Delta x = \Delta y = 0.5$ nm. See the caption to Figure 3.9 for further details.

(a)

(b)

FIG. 3.13. A comparison between the light control pulses, $E_z^{(i)}$ and $E_z^{(in)}$, designed, respectively, by the conventional and the present Maxwell-Schrödinger hybrid simulation for the size of the cross section of the tube $\Delta x = \Delta y = 1.5$ nm. See the caption to Figure 3.9 for further details.

3.3 Disucussion

In this section we have studied a system of an electron confined in a quasi-one-dimensional electrostatic potential and examined in detail the effect of the near field created by the electron excited by the incident laser pulse. We have focused particularly on a light control pulse that could transfer completely the probability density of the ground state to the objective first excited state. Relying on the Maxwell-Schrödinger hybrid simulation, we have first tested the control ability of the conventional light control pulse that has been designed without taking into account the modification of the incident laser field by the excited electron. The results show that the conventional pulse could somehow control the system in the case where the electron density is small. On the other hand, in the case with a high electron density, the conventional pulse can hardly transfer the system from the ground state to the objective state.

We have then proposed a novel method to design a light control pulse by extending the conventional method so as to incorporate the effect of the local modification of the laser field by the induced radiation from the excited electron. This new light control pulse has been examined and shown to control the quantum states ideally not only for the case with a small electron density but also for the case with a high electron density. These results indicate that even a single electron can create a locally strong radiation field in the vicinity of the region where its wave function extends, that could make the conventional method impractical in designing light control pulses. Strictly speaking, the present results can be applicable only to the studied model of an electron confined in a quasi-one-dimensional nanostructure, simulating quantum dots or nanowires. The significance of the induced radiation could, however, be equally applicable to atomic and molecular systems in general, since their average electron density is comparable or even larger than that of the present model. For example, in the case of the hydrogen atom in its $2p$ state one electron is confined in a sphere with the radius of 4 times Bohr radius, i.e., 0.21 nm. Therefore, its average electron density is estimated to be 4.0×10^9 C/m^3. On the other hand, the average electron density of the present model for the case when the conventional pulse is of no practical use is 1.8×10^9 C/m^3 and is thus smaller than the case for the hydrogen atom.

Finally, we would like to comment on a possibility of observing the effect of local modification of the incident laser field by the excitation of electron in actual experimentations. Recent experimental developments in generating ultrashort laser pulses have already enabled us to shape the temporal profile of the laser pulses in an almost arbitrary way within the range of, of course, coverage of their frequency spectrum. Therefore, the control ability of the laser pulses obtained by the present Maxwell-Schrödinger hybrid scheme and by the conventional one can be examined by implementing them into a pump-probe type of experimentations in which a target quantum system is pumped by the control pulse whose final state is then monitored by a probe

pulse. A promising target system may be a simple atom or a molecule with only a small number of active electrons for which the accurate Maxwell-Schrödinger hybrid simulation can be performed.

4 Conclusions

In this dissertation the author has studied where phenomena occurred in the "*mesoscopic*" region which is expediently defined to involve not only the classical- but also quantum-theories, by utilizing recently developed highly-accurate hybrid simulation to investigate the light-matter interaction. Since both of the Maxwell and Schrödinger equations could be successfully coupled in the simulation, the hybrid scheme could realize very efficient and precise computation and has been successfully applied to two problems constructed by light-matter interaction: (i) many-electron systems and (ii) single-electron ones.

The former problem has been strongly motivated in terms of theoretical modelization of plasmonic devices which have currently attracted great attention as one of important roles in next generation key information technologies and been modeled so far by solely the classical physics despite the fact that the quantum mechanical effects for the devices have been actually observed in very recent experimental works. Therefore, the validity of such conventional classical simulation, namely a Maxwell-Newton scheme, has been challenged by making a comparison with the hybrid simulation of Maxwell-Schrödinger equations, where the author especially has focused on the structure of the electrostatic potentials that confine electrons. The resultant trend has clearly represented the applicable scope of the conventional Maxwell-Newton scheme whose simulated results coincides with precise one of our Maxwell-Schrödinger scheme for the purely harmonic potential structure while qualitatively deviates for the potentials characterized by locally- or globally anharmonicities, due to the some typical quantum mechanical effects: tunnelling or dephasing. These things explicitly indicate the need of Maxwell-Schrödinger algorithm for the simulation of the plasmonic devices.

Another problem, that the author addressed, has been motivated by the design of light control pulses which can adjust the discrete quantum levels of particles in matter to arbitrary desired one, namely have potential ability to realize q-bit for quantum computers that is significantly faster than classical computers so far. The conventional schemes to design the pulses are based on the assumption that the electromagnetic field near the target system is not disturbed by the excitation of electrons, going against a sense of near field optics. Therefore, in order to verify this assumption actually, the author has firstly tried to simulate the near field generated by a single electron set as a target system irradiated with the conventional designing pulse, by relying on the use of precise Maxwell-Schrödinger hybrid simulation. As a result the conventional pulse could not stably control the electronic state since the strong near field is generated around the electronic wave packet and the field significantly modifies the original incoming pulse. Furthermore, it has been revealed that the intensity of the near field deeply depends on the density of the electron wave packet which determines that of polarization current. Hence the author has then proposed a

novel designing scheme to obtain light control pulses which precisely considers such near field effects and could stably control the electronic state. These clarified trends indicate that the Maxwell-Schrödinger algorithm should be indispensable for such problems.

Appendix

In this appendix we present mathematical formulas to be used for developing computational codes for performing the Maxwell-Schrödinger hybrid simulation to solve 3D-1D problems.

(A) FDTD

Our hybrid simulation solves the coupled Maxwell and Schrödinger equations simultaneously as described by Eqs. (3.1) - (3.3). It needs to evaluate **E**, **H**, **A**, **J**, φ, and ψ at every time steps. All these functions are placed on the space-time grid points as displayed in Figure A.1. The following recursion relations are used to update each component of the discretized **E** and **H**:

$$E_x^{n+1}\left(i+\frac{1}{2},j,k\right) = E_x^n\left(i+\frac{1}{2},j,k\right)$$

$$+\frac{\Delta t}{\varepsilon_0 \Delta y}\left\{H_z^{n+\frac{1}{2}}\left(i+\frac{1}{2},j+\frac{1}{2},k\right) - H_z^{n+\frac{1}{2}}\left(i+\frac{1}{2},j-\frac{1}{2},k\right)\right\}$$

$$-\frac{\Delta t}{\varepsilon_0 \Delta z}\left\{H_y^{n+\frac{1}{2}}\left(i+\frac{1}{2},j,k+\frac{1}{2}\right) - H_y^{n+\frac{1}{2}}\left(i+\frac{1}{2},j,k-\frac{1}{2}\right)\right\}, \tag{A.1}$$

$$E_y^{n+1}\left(i,j+\frac{1}{2},k\right) = E_y^n\left(i,j+\frac{1}{2},k\right)$$

$$+\frac{\Delta t}{\varepsilon_0 \Delta z}\left\{H_x^{n+\frac{1}{2}}\left(i,j+\frac{1}{2},k+\frac{1}{2}\right) - H_x^{n+\frac{1}{2}}\left(i,j+\frac{1}{2},k-\frac{1}{2}\right)\right\}$$

$$-\frac{\Delta t}{\varepsilon_0 \Delta x}\left\{H_z^{n+\frac{1}{2}}\left(i+\frac{1}{2},j+\frac{1}{2},k\right) - H_z^{n+\frac{1}{2}}\left(i-\frac{1}{2},j+\frac{1}{2},k\right)\right\}, \tag{A.2}$$

$$E_z^{n+1}\left(i,j,k+\frac{1}{2}\right) = E_z^n\left(i,j,k+\frac{1}{2}\right)$$

$$+\frac{\Delta t}{\varepsilon_0 \Delta x}\left\{H_y^{n+\frac{1}{2}}\left(i+\frac{1}{2},j,k+\frac{1}{2}\right) - H_y^{n+\frac{1}{2}}\left(i-\frac{1}{2},j,k+\frac{1}{2}\right)\right\}$$

$$-\frac{\Delta t}{\varepsilon_0 \Delta y}\left\{H_x^{n+\frac{1}{2}}\left(i,j+\frac{1}{2},k+\frac{1}{2}\right) - H_x^{n+\frac{1}{2}}\left(i,j-\frac{1}{2},k+\frac{1}{2}\right)\right\} - \frac{\Delta t}{\varepsilon_0}J_z^{n+\frac{1}{2}}\left(i,j,k+\frac{1}{2}\right), \tag{A.3}$$

$$
H_x^{n+1}\left(i, j+\frac{1}{2}, k+\frac{1}{2}\right) = H_x^n\left(i, j+\frac{1}{2}, k+\frac{1}{2}\right)
$$

$$
-\frac{\Delta t}{\mu_0 \Delta y}\left\{E_z^{n+\frac{1}{2}}\left(i, j+1, k+\frac{1}{2}\right) - E_z^{n+\frac{1}{2}}\left(i, j, k+\frac{1}{2}\right)\right\}
$$

$$
+\frac{\Delta t}{\mu_0 \Delta z}\left\{E_y^{n+\frac{1}{2}}\left(i, j+\frac{1}{2}, k+1\right) - E_y^{n+\frac{1}{2}}\left(i, j+\frac{1}{2}, k\right)\right\}, \qquad \text{(A.4)}
$$

$$
H_y^{n+1}\left(i+\frac{1}{2}, j, k+\frac{1}{2}\right) = H_y^n\left(i+\frac{1}{2}, j, k+\frac{1}{2}\right)
$$

$$
-\frac{\Delta t}{\mu_0 \Delta z}\left\{E_x^{n+\frac{1}{2}}\left(i+\frac{1}{2}, j, k+1\right) - E_x^{n+\frac{1}{2}}\left(i+\frac{1}{2}, j, k\right)\right\}
$$

$$
+\frac{\Delta t}{\mu_0 \Delta x}\left\{E_z^{n+\frac{1}{2}}\left(i+1, j, k+\frac{1}{2}\right) - E_z^{n+\frac{1}{2}}\left(i, j, k+\frac{1}{2}\right)\right\}, \qquad \text{(A.5)}
$$

$$
H_z^{n+1}\left(i+\frac{1}{2}, j+\frac{1}{2}, k\right) = H_z^n\left(i+\frac{1}{2}, j+\frac{1}{2}, k\right)
$$

$$
-\frac{\Delta t}{\mu_0 \Delta x}\left\{E_y^{n+\frac{1}{2}}\left(i+1, j+\frac{1}{2}, k\right) - E_y^{n+\frac{1}{2}}\left(i, j+\frac{1}{2}, k\right)\right\}
$$

$$
+\frac{\Delta t}{\mu_0 \Delta y}\left\{E_x^{n+\frac{1}{2}}\left(i+\frac{1}{2}, j+1, k\right) - E_x^{n+\frac{1}{2}}\left(i+\frac{1}{2}, j, k\right)\right\}. \qquad \text{(A.6)}
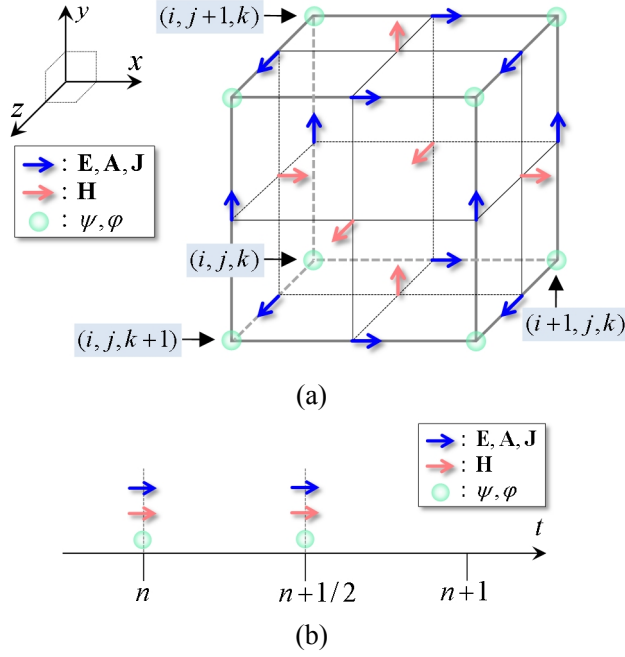$$

FIG. A.1. Space- and time-configurations[(a) and (b)] of the physical quantities on the spatiotemporal grid in the Maxwell-Schrödinger hybrid simulation. The set of symbols $i, j,$ and k represents indices to specify the grid points on the x-, y-, and z-axes, respectively, while n specifies the grid points on the time axis.

The recursion relations for updating the vector and scalar potentials, $\mathbf{A}$ and φ, are obtained by applying the second-order accurate difference formula to the time- and space-derivatives to Eqs. (3.4) and (3.5) as.

$$A_x^{n+1}\left(i+\frac{1}{2}, j, k\right) = A_x^n\left(i+\frac{1}{2}, j, k\right)$$
$$-\frac{\Delta t}{\Delta x}\left\{\varphi^{n+\frac{1}{2}}(i+1, j, k) - \varphi^{n+\frac{1}{2}}(i, j, k)\right\} - \Delta t E_x^{n+\frac{1}{2}}\left(i+\frac{1}{2}, j, k\right), \tag{A.7}$$

$$A_y^{n+1}\left(i, j+\frac{1}{2}, k\right) = A_y^n\left(i, j+\frac{1}{2}, k\right)$$
$$-\frac{\Delta t}{\Delta y}\left\{\varphi^{n+\frac{1}{2}}(i, j+1, k) - \varphi^{n+\frac{1}{2}}(i, j, k)\right\} - \Delta t E_y^{n+\frac{1}{2}}\left(i, j+\frac{1}{2}, k\right), \tag{A.8}$$

$$A_z^{n+1}\left(i, j, k+\frac{1}{2}\right) = A_z^n\left(i, j, k+\frac{1}{2}\right)$$
$$-\frac{\Delta t}{\Delta z}\left\{\varphi^{n+\frac{1}{2}}(i, j, k+1) - \varphi^{n+\frac{1}{2}}(i, j, k)\right\} - \Delta t E_z^{n+\frac{1}{2}}\left(i, j, k+\frac{1}{2}\right), \tag{A.9}$$

54

$$\varphi^{n+1}(i,j,k) = \varphi^n(i,j,k)$$

$$-\frac{\Delta t}{\mu_0\varepsilon_0}\left[\frac{1}{\Delta x}\left\{A_x^{n+\frac{1}{2}}\left(i+\frac{1}{2},j,k\right)-A_x^{n+\frac{1}{2}}\left(i-\frac{1}{2},j,k\right)\right\}\right.$$

$$+\frac{1}{\Delta y}\left\{A_y^{n+\frac{1}{2}}\left(i,j+\frac{1}{2},k\right)-A_y^{n+\frac{1}{2}}\left(i,j-\frac{1}{2},k\right)\right\}$$

$$\left.+\frac{1}{\Delta z}\left\{A_z^{n+\frac{1}{2}}\left(i,j,k+\frac{1}{2}\right)-A_z^{n+\frac{1}{2}}\left(i,j,k-\frac{1}{2}\right)\right\}\right]. \tag{A.10}$$

The recursion relation for the time-dependent electron wave packet ψ is obtained by applying the Schrödinger FDTD method to Eq. (3.1) as

$$\psi_{real}^{n+1}(k)=\psi_{real}^n(k)-\frac{\hbar\Delta t}{2m}\alpha_k\left\{\psi_{imag}^{n+\frac{1}{2}}(k)\right\}$$

$$+\frac{q\Delta t}{2m}\beta_k\left[\frac{1}{2}\left\{A_z^{n+\frac{1}{2}}\left(i_T,j_T,k+\frac{1}{2}\right)+A_z^{n+\frac{1}{2}}\left(i_T,j_T,k-\frac{1}{2}\right)\right\}\psi_{real}^{n+1/2}(k)\right]$$

$$+\frac{q\Delta t}{4m}\left\{A_z^{n+\frac{1}{2}}\left(i_T,j_T,k+\frac{1}{2}\right)+A_z^{n+\frac{1}{2}}\left(i_T,j_T,k-\frac{1}{2}\right)\right\}\beta_k\left\{\psi_{real}^{n+\frac{1}{2}}(k)\right\}$$

$$+\frac{\Delta t}{\hbar}\left[\frac{q^2}{8m}\left\{A_z^{n+\frac{1}{2}}\left(i_T,j_T,k+\frac{1}{2}\right)+A_z^{n+\frac{1}{2}}\left(i_T,j_T,k-\frac{1}{2}\right)\right\}^2\right.$$

$$\left.+q\varphi^{n+\frac{1}{2}}(i_T,j_T,k)+V(k)\right]\psi_{imag}^{n+\frac{1}{2}}(k), \tag{A.11}$$

$$\psi_{imag}^{n+1}(k)=\psi_{imag}^n(k)+\frac{\hbar\Delta t}{2m}\alpha_k\left\{\psi_{real}^{n+\frac{1}{2}}(k)\right\}$$

$$+\frac{q\Delta t}{2m}\beta_k\left[\frac{1}{2}\left\{A_z^{n+\frac{1}{2}}\left(i_T,j_T,k+\frac{1}{2}\right)+A_z^{n+\frac{1}{2}}\left(i_T,j_T,k-\frac{1}{2}\right)\right\}\psi_{imag}^{n+1/2}(k)\right]$$

$$+\frac{q\Delta t}{4m}\left\{A_z^{n+\frac{1}{2}}\left(i_T,j_T,k+\frac{1}{2}\right)+A_z^{n+\frac{1}{2}}\left(i_T,j_T,k-\frac{1}{2}\right)\right\}\beta_k\left\{\psi_{imag}^{n+\frac{1}{2}}(k)\right\}$$

$$-\frac{\Delta t}{\hbar}\left[\frac{q^2}{8m}\left\{A_z^{n+\frac{1}{2}}\left(i_T,j_T,k+\frac{1}{2}\right)+A_z^{n+\frac{1}{2}}\left(i_T,j_T,k-\frac{1}{2}\right)\right\}^2\right.$$

$$\left.+q\varphi^{n+\frac{1}{2}}(i_T,j_T,k)+V(k)\right]\psi_{real}^{n+\frac{1}{2}}(k), \tag{A.12}$$

where ψ_{real} and ψ_{imag} represent, respectively, the real and imaginary parts of the wave function ψ with i_T and j_T denoting the indices to specify the position of the tube on the *x-y* plane shown in Figure 3.1.
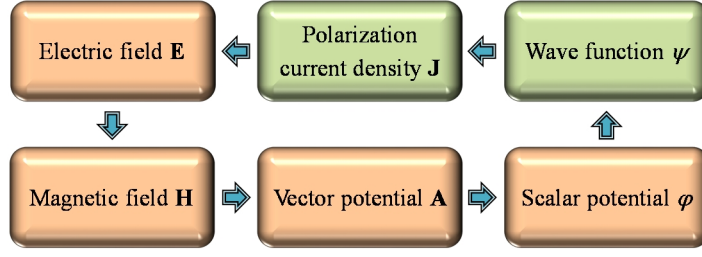
FIG. A.2. A schematic illustration of the computational algorithm for updating the physical quantities in the Maxwell-Schrödinger hybrid simulation.

The following boundary conditions have been utilized to the discretized wave function throughout the present study:

$$\psi(1) = \psi(2) = \psi(3) = \psi(k_{max}) = \psi(k_{max} - 1) = \psi(k_{max} - 2) = 0, \tag{A.13}$$

where perfectly matched layers[30] have also been used to the boundary condition for the electromagnetic fields.

The polarization current density of Eq. (3.6) is evaluated by the following expressions with the β operator defined by Eq. (2.12) to compute the first-order derivative of $\partial/\partial z$ as

$$J_z^{n+\frac{1}{2}}\left(k + \frac{1}{2}\right) = \frac{1}{2}\left\{J_z^{n+\frac{1}{2}}(k+1) + J_z^{n+\frac{1}{2}}(k)\right\}, \tag{A.14}$$

$$J_z^{n+\frac{1}{2}}(k) = \frac{q\hbar}{m}\left[\psi_{real}^{n+\frac{1}{2}}(k)\beta_k\left\{\psi_{imag}^{n+\frac{1}{2}}(k)\right\} - \psi_{imag}^{n+\frac{1}{2}}(k)\beta_k\left\{\psi_{real}^{n+\frac{1}{2}}(k)\right\}\right]$$

$$-\frac{q^2}{2m}\left[\left\{\psi_{real}^{n+\frac{1}{2}}(k)\right\}^2 + \left\{\psi_{imag}^{n+\frac{1}{2}}(k)\right\}^2\right]\left\{A_z^{n+\frac{1}{2}}\left(i_T, j_T, k + \frac{1}{2}\right) + A_z^{n+\frac{1}{2}}\left(i_T, j_T, k - \frac{1}{2}\right)\right\}. \tag{A.15}$$

The Maxwell-Schrödinger hybrid simulation can be realized by using these equations (A1) - (A15) in the manner as illustrated schematically in Figure A.2.

(B)   Novel design method for a light control pulse

Our new method of designing light control pulses is based on Eqs. (3.22) and (3.23). First, the time-dependent wave function ψ obtained by solving the coupled Maxwell-Schrödinger equations needs to be transformed into $\widetilde{\psi}'$ by the discretized formula of Eq. (3.23) as

$$\widetilde{\psi}'^{n+\frac{1}{2}}_{real}(k) = \cos\left[\frac{q}{2\hbar}\left\{A_z^{n+\frac{1}{2}}\left(i_T, j_T, k+\frac{1}{2}\right) + A_z^{n+\frac{1}{2}}\left(i_T, j_T, k-\frac{1}{2}\right)\right\}Z(k)\right]\psi^{n+\frac{1}{2}}_{real}$$

$$+\sin\left[\frac{q}{2\hbar}\left\{A_z^{n+\frac{1}{2}}\left(i_T, j_T, k+\frac{1}{2}\right) + A_z^{n+\frac{1}{2}}\left(i_T, j_T, k-\frac{1}{2}\right)\right\}Z(k)\right]\psi^{n+\frac{1}{2}}_{imag}, \qquad \text{(A.16)}$$

$$\widetilde{\psi}'^{n+\frac{1}{2}}_{imag}(k) = -\sin\left[\frac{q}{2\hbar}\left\{A_z^{n+\frac{1}{2}}\left(i_T, j_T, k+\frac{1}{2}\right) + A_z^{n+\frac{1}{2}}\left(i_T, j_T, k-\frac{1}{2}\right)\right\}Z(k)\right]\psi^{n+\frac{1}{2}}_{real}$$

$$+\cos\left[\frac{q}{2\hbar}\left\{A_z^{n+\frac{1}{2}}\left(i_T, j_T, k+\frac{1}{2}\right) + A_z^{n+\frac{1}{2}}\left(i_T, j_T, k-\frac{1}{2}\right)\right\}Z(k)\right]\psi^{n+\frac{1}{2}}_{imag}, \qquad \text{(A.17)}$$

where $Z(k)$ represents the discretized z axis. Then, the new light control pulse Ez(in) is obtained by the discretized formula of Eq. (3.24) as

$$E_z^{(in)^{n+\frac{1}{2}}} = -2\frac{qE_0\Delta z^2}{m}\left[\sum_{k=1}^{k_{\max}}\left\{\widetilde{\psi}'^{n+\frac{1}{2}}_{real}(k)\psi_\zeta(k)\right\} \times \sum_{k=1}^{k_{\max}}\left\{Z(k)\widetilde{\psi}'^{n+\frac{1}{2}}_{imag}(k)\psi_\zeta(k)\right\}\right.$$

$$\left.-\sum_{k=1}^{k_{\max}}\left\{\widetilde{\psi}'^{n+\frac{1}{2}}_{imag}(k)\psi_\zeta(k)\right\} \times \sum_{k=1}^{k_{\max}}\left\{Z(k)\widetilde{\psi}'^{n+\frac{1}{2}}_{real}(k)\psi_\zeta(k)\right\}\right]. \qquad \text{(A.18)}$$

List of references

[1] Ministry of Internal Affairs and Communications, White Paper on Local Public Finance, 2015 -Illustrated-. Tokyo, Japan: Nikkei Printing Inc., 2015.

[2] J. Dintinger, S. Klein, F. Bustos, W. L. Barnes, and T. W. Ebbesen, "Strong coupling between surface plasmon-polaritons and organic molecules in subwavelength hole arrays," *Physical Review B*, vol. 71, pp. 035424-1-035424-5, Jan. 2005.

[3] E. Ozbay, "Plasmonics: Merging Photonics and Electronics at Nanoscale Dimensions," *Science*, vol. 311, pp. 189-193, Jan. 2006.

[4] K. Nakagawa, A. Tajiri, K. Tamura, S. Toriumi, Y. Ashizawa, A. Tsukamoto, A. Itoh, Y. Sasaki, S. Saito, M. Takahashi, and S. Ohnuki, "Thermally Assisted Magnetic Recording Applying Optical Near Field with Ultra Short-Time Heating," *Journal Journal of the Magnetics Society of Japan*, vol. 37, no. 3-2, pp. 119-122, Mar. 2013.

[5] P. Benioff, "The Computer as a Physical System: A Microscopic Quantum Mechanical Hamiltonian Model of Computers as Represented by Turing Machines," *Journal of Statistical Physics*, vol. 22, no. 5, pp. 563-591, May 1980.

[6] R. Feynman, "Simulating Physics with Computers," *International Journal of Theoretical Physics*, vol. 21, no. 6, pp. 467-488, Jun. 1982.

[7] P. W. Shor, "Algorithms for Quantum Computation: Discrete Logarithms and Factoring," *Proceedings of 35th Annual Symposium on Foundations of Computer Science*, pp. 124-134, Santa Fe, New Mexico, USA, Nov. 1994.

[8] L. M. K. Vandersypen, M. Steffen, G. Breyta, C. S. Yannoni, M. H. Sherwood, and I. L. Chuang, "Experimental realization of Shor's quantum factoring algorithm using nuclear magnetic resonance," *Nature*, vol. 414, pp. 883-887, Dec. 2001.

[9] J. Clarke and F. K. Wilhelm, "Superconducting quantum bits," *Nature*, vol. 453, pp.1031-1042, Jun. 2008.

[10] D. Loss and D. P. DiVincenzo, "Quantum computation with quantum dots," *NaturePhysical Review A*, vol. 57, no. 1, pp.120-126, Jan. 1998.

[11] C. M. Tesch, L. Kurtz, and R. de Vivie-Riedle, "Applying optimal control theory for elements of quantum computation in molecular systems," *Chemical Physics Letters*, vol. 343, pp. 633-641, Aug. 2001.

[12] J. P. Palao and R. Kosloff, "Quantum computing by an optimal control algorithm for unitary transformations," *Physical Review Letters*, vol. 89, pp. 188301-1-188301-4, Oct. 2002.

[13] S. Suzuki, K. Mishima, and K. Yamashita, "Ab initio study of optimal control of ammonia molecular vibrational wavepackets: Towards molecular quantum computing," *Chemical Physics Letters*, vol. 410, pp. 358-364, Apr. 2005.

[14] T. Takeuchi, S. Ohnuki, and T. Sako, "Comparison between Maxwell–Schrödinger and

Maxwell–Newton hybrid simulations for multi-well electrostatic potential," *IEEE Journal of Quantum Electronics*, vol.50, no.5, pp.334-339, May 2014.

[15] T. Takeuchi, S. Ohnuki, and T. Sako, "Hybrid simulation of Maxwell-Schrödinger equations for multi-physics problems characterized by anharmonic electrostatic potential(Invited Paper)," *Progress In Electromagnetics Research*, vol.148, pp.73-82, Jul. 2014.

[16] T. Takeuchi, S. Ohnuki, and T. Sako, "Maxwell-Schrödinger hybrid simulation for optically controlling quantum states: A scheme for designing control pulses," *Physical Review A*, vol.91, pp.003400-1-003400-13, Mar. 2015.

[17] I. P. Christov, M. M. Murnane, and H. C. Kapteyn, "Generation and propagation of attosecond x-ray pulses in gaseous media," *Physical Review A*, vol. 57, no. 4, pp. R2285-R2288, Apr. 1998.

[18] E. Lorin, S. Chelkowski, and A. D. Bandrauk, "A numerical Maxwell–Schrödinger model for intense laser-matter interaction and propagation," *Computer Physics Communications*, vol. 177, no.12, pp. 908-932, Jul. 2007.

[19] L. Pierantoni, D. Mencarelli, and T. Rozzi, "A new 3-D transmission line matrix scheme for the combined Schrödinger–Maxwell problem in the electronic/electromagnetic characterization of nanodevices," *IEEE Transactions on Microwave Theory and Techniques*, vol. 56, no. 3, pp. 654-662, Mar. 2008.

[20] J. A. Scholl, A. L. Koh, and J. A. Dionne, "Quantum plasmon resonances of individual metallic nanoparticles," *Nature*, vol. 483, pp. 421-427, Mar. 2012.

[21] C. Ciracì, R. T. Hill, J. J. Mock, Y. Urzhumov, A. I. Fernández-Domínguez, S. A. Maier, J. B. Pendry, A. Chilkoti, and D. R. Smith, "Probing the ultimate limits of plasmonic enhancement," *Science*, vol. 337, no. 6098, pp. 1072-1074, Aug. 2012.

[22] C. Ciracì, J. B. Pendry, and D. R. Smith, "Hydrodynamic Model for Plasmonics: A Macroscopic Approach to a Microscopic Problem," *ChemPhysChem*, vol. 14, pp. 1109-1116, Apr. 2013.

[23] Y. Luo, A. I. Fernandez-Dominguez, A. Wiener, S. A. Maier, and J. B. Pendry, "Surface Plasmons and Nonlocality: A Simple Model," *Physical Review Letters*, vol. 111, pp. 093901-1-093901-5, Aug. 2013.

[24] D. Meshulach and Y. Silberberg, "Coherent quantum control of two-photon transitions by a femtosecond laser pulse," *Nature*, vol. 396, pp. 239-242, Nov. 1998.

[25] H. Rabitz, R. de Vivie-Riedle, M. Motzkus, and K. Kompa, "Whither the Future of Controlling Quantum Phenomena?," *Science*, vol. 288, no. 5467, pp. 824-828, May. 2000.

[26] D. Brinks, F. D. Stefani, F. Kulzer, R. Hildner, T. H. Taminiau, Y. Avlasevich, K. Müllen, and N. F. van Hulst, "Visualizing and controlling vibrational wave packets of single molecules," *Nature*, vol. 465, pp. 905-908, Apr. 2010.

[27] B. Kohler, V. V. Yakovlev, J. Che, J. L. Krause, M. Messina, K. R. Wilson, N. Schwentner,

R. M. Whitnell, and Y.-J. Yan, "Quantum control of wave packet evolution with tailored femtosecond pulses," *Physical Review Letters*, vol. 74, no. 17, pp. 3360-3363, Apr. 1995.

[28] T. Brixner, N. H. Damrauer, P. Niklaus, and G. Gerber, "Photoselective adaptive femtosecond quantum control in the liquid phase," *Nature*, vol. 414, pp. 57-60, Nov. 2001.

[29] C. Daniel1, J. Full, L. González, C. Lupulescu, J. Manz, A. Merli, Š. Vajda, and L. Wöste, "Deciphering the Reaction Dynamics Underlying Optimal Control Laser Fields," *Science*, vol. 299, no. 5606, pp. 536-539, Jan. 2003.

[30] A. P. Peirce, M. A. Dahleh, and H. Rabitz, "Optimal control of quantum-mechanical systems: Existence, numerical approximation, and applications," *Physical Review A*, vol. 37, no. 12, pp. 4950-4964, Jun. 1988.

[31] S. Shi and H. Rabitz, "Quantum mechanical optimal control of physical observables in microsystems," *The Journal of Chemical Physics*, vol. 92, no. 1, pp. 364-376, Jan. 1990.

[32] Y. Ohtsuki, H. Kono, and Y. Fujimura, "Quantum control of nuclear wave packets by locally designed optimal pulses," *The Journal of Chemical Physics*, vol. 109, no. 21, pp. 9318-9331, Dec. 1998.

[33] A. Lewis and K. Lieberman, "Near-field optical imaging with a non-evanescently excited high-brightness light source of sub-wavelength dimensions," *Nature*, vol. 354, pp. 214-216, Nov. 1991.

[34] F. Zenhausern, M. P. O'Boyle, and H. K. Wickramasinghe, "Apertureless near-field optical microscope," *Applied Physics Letters*, vol. 65, no. 13, pp. 1623-1625, Sep. 1994.

[35] L. Novotny, D. W. Pohl, and P. Regli, "Light propagation through nanometer-sized structures: the two-dimensional-aperture scanning near-field optical microscope," *Journal of the Optical Society of America A*, vol. 11, no. 6, pp. 1768-1779, Jun. 1994.

[36] K. S. Yee, "Numerical Solution of initial boundary value problems involving Maxwell's equations in isotropic media," *IEEE Transactions on Antennas and Propagation*, vol. 14, pp. 302–307, May 1996.

[37] A. Taflove and S. C. Hagness, *Computational Electrodynamics the Finite-Difference Time-Domain Method*, 3rd ed. Boston, MA, USA: Artech House, 2005.

[38] A. Soriano, E. A. Navarro, J. A. Porti, and V. Such, "Analysis of the finite difference time domain technique to solve the Schrödinger equation for quantum devices," *Journal of Applied Physics*, vol. 95, no. 12, pp. 8011-8018, Jun. 2004.

[39] D. M. Sullivan, *Electromagnetic Simulation Using the FDTD Method*. New York, USA: IEEE Press Series on RF and Microwave Technology, 2000.

[40] T. Yamaguchi and T. Hinata, "Optical near-field analysis of spherical metals: Application of the FDTD method combined with the ADE method," Optics Express, vol. 15, no. 18, pp. 11481-11491, Sep. 2007.

[41] C. Cohen-Tannoudji, J. Dupont-Roc, and C. Crynberg, Atom-Photon Interactions: Basic

Processes and Applications. Weinheim, Germany: Wiley-VCH, 2004.

[42] N. F. Johnson, "Quantum dots: few-body, low-dimensional systems," *Journal of Physics: Condensed Matter*, vol. 7, no. 6 pp. 965-989, Feb. 1995.

[43] T. Sako and G. H. F. Diercksen, "Spectra and correlated wave functions of two electrons confined in a quasi-one-dimensional nanostructure," *Physical Review B*, vol. 75, pp. 115413-1-115413-12, Mar. 2007.

[44] T. Sako and G. H. F. Diercksen, "Understanding the spectra of a few electrons confined in a quasi-one-dimensional nanostructure," *Journal of Physics: Condensed Matter*, vol. 20, no. 15, pp. 155202-1-155202-3, Ma. 2008.